Simulation and Design of 25 kW Modular Dual Active Bridge(DAB) DC-DC Converter for EV Chargers

M.Tech Thesis

by

Vishwarup Datta

CENTRE FOR ELECTRIC VEHICLE AND INTELLIGENT TRANSPORT SYSTEMS

INDIAN INSTITUTE OF TECHNOLOGY INDORE

May 2025

Simulation and Design of 25 kW Modular Dual Active Bridge(DAB) DC-DC Converter for EV Chargers

A THESIS

Submitted in partial fulfillment of the

requirements for the award of the degree

of

Master of Technology

by

Vishwarup Datta

2302106008

CENTRE FOR ELECTRIC VEHICLE AND INTELLIGENT TRANSPORT SYSTEMS

INDIAN INSTITUTE OF TECHNOLOGY INDORE

May 2025

INDIAN INSTITUTE OF TECHNOLOGY INDORE

CANDIDATE'S DECLARATION

I hereby certify that the work which is being presented in the thesis entitled **Simulation and Design of 25 kW Modular Dual Active Bridge(DAB) DC-DC Converter for EV Chargers** in the partial fulfillment of the requirements for the award of the degree of **Master of Technology** and submitted in the **Center for Electric Vehicle and Intelligent Transport System, Indian Institute of Technology Indore,** is an authentic record of my own work carried out during the period from July 2024 to May 2025 under the supervision of Prof. Amod C. Umarikar, Indian Institute of Technology Indore, India.

The matter presented in this thesis has not been submitted by me for the award of any other degree of this or any other institute.

Vishwarup Datta
28/5/2025

Signature of the Student with Date

(Vishwarup Datta)

This is to certify that the above statement made by the candidate is correct to the best of my knowledge.

29/05/2025

Signature of Thesis Supervisor with Date

(Prof. Amod C. Umarikar)

ACKNOWLEDGEMENT

First and foremost, I would like to express my heartfelt gratitude to my supervisor, Prof.Amod C. Umarikar , for his invaluable guidance, constant support, and insightful suggestions throughout the course of this research. His encouragement and expertise have been instrumental in shaping both the direction and the quality of this work.

I would also like to thank my friends and peers at IIT Indore for their continuous support, helpful discussions, and for creating a collaborative and motivating environment that made this journey enriching and enjoyable.

Lastly, I am deeply thankful to my parents and family for their unconditional love, patience, and unwavering support. Their encouragement has been my strongest pillar throughout my academic journey.

This thesis would not have been possible without the contribution and support of all these individuals.

Vishwarup Datta

Dedicated to My Family

ABSTRACT

The growing demand for efficient, scalable, and reliable electric vehicle (EV) charging infrastructure has catalyzed interest in advanced power electronics topologies. Among these, the Dual Active Bridge (DAB) converter stands out due to its bidirectional power flow capability, galvanic isolation, and high efficiency across various operating conditions. However, a modular architecture for DAB converters becomes essential as power levels and complexity increase, particularly in fast-charging applications. This Thesis advocates for the use of a modular DAB converter architecture in EV chargers, emphasizing its advantages in scalability, fault tolerance, thermal management, and ease of maintenance. A modular approach enables the construction of high-power chargers by paralleling multiple lower-power DAB modules, offering design flexibility and cost-effective scaling. This not only supports future growth in EV adoption and charging demands but also simplifies the customization of charger output power for different applications. Additionally, redundancy can be incorporated into the modular design, allowing the charger to continue operating at reduced capacity in the event of a module failure, thereby improving system reliability and availability. Modular DAB systems also facilitate distributed thermal management and reduce current stress on individual components, enhancing overall efficiency and lifespan. Furthermore, modularity simplifies maintenance and replacement procedures, minimizing downtime and operational disruptions. In conclusion, the modular architecture of the DAB converter aligns well with the evolving requirements of EV charging infrastructure. It provides a robust and adaptable platform that can meet the increasing power demands while ensuring high efficiency, operational resilience, and long-term serviceability. As the EV market continues to expand, adopting modular DAB converters in charging stations will be pivotal in building a sustainable and future-ready energy ecosystem.

Contents

List of Figures

List of Tables

Acronyms

DAB	Dual Active Bridge
DPS	Double Phase Shift
EPS	Extended Phase Shift
EV	Electric Vehicle
IGBT	Insulated Gate Bipolar Transistor
MOSFET	Metal Oxide Semiconductor Field Effect Transistor
ISOP	Input Series Output Parallel
SISO	Single Input Single Output
SPS	Single Phase Shift
TPS	Triple Phase Shift
MIMO	Multiple Input Multiple Output
ZVS	Zero Voltage Switching

Chapter 1

Introduction

1.1 Context and Motivation

Electric vehicles (EV) have emerged as a promising solution to mitigate the environmental impacts of transportation, reduce dependence on fossil fuels, and promote sustainable mobility. In the past few years, governments, manufacturers and consumers are increasingly embracing EVs as a viable alternative to internal combustion engine vehicles. However, despite the numerous benefits of electric vehicles, there are still some challenges and limitations that hinder their widespread adoption.

The EV's restricted energy supply, which is solely reliant on the battery's capacity, limit its range and prevent it from being used for long-distance driving. Since the shift to mainstream EV adoption depends not only on improvements in vehicle technology but also substantially on the development of reliable charging infrastructure and charging technologies, another obstacle is the scarcity of public charging stations.

The adoption of electric vehicles continues to grow and it is important to ensure that charging infrastructure is able to support the increasing demand for electricity and do so in a way that is efficient, reliable, and sustainable. To address these challenges, researchers and engineers are continuously exploring advanced charging technologies

and power electronics solutions.

Electric car adoption is still on the rise, therefore it's critical to make sure that charging infrastructure can keep up with the growing demand for electricity in a sustainable, dependable, and effective manner. Researchers and engineers are constantly looking into cutting-edge charging technologies and power electronics solutions to overcome these issues.

A proposed architecture called the **Modular Dual Active Bridge (Modular DAB)** aims to improve fault tolerance, scalability, and efficiency in high-power applications. By modularly connecting several DAB converter modules, this method enables more flexible system design, simpler maintenance, and improved thermal control. The redundancy that modular DAB converters offer allows them to continue functioning even in the case of a partial system failure, which makes them especially appropriate for high-reliability power systems like next-generation EV charging infrastructure.

1.2 Objectives

The theory, design, closed loop control, and simulation of DAB are examined in further detail in this thesis. Likewise, the modular DAB architecture is examined and its closed loop control simulation is carried out.

1.3 Thesis Structure

This thesis is divided into 6 chapters

- **Chapter 2** In this chapter we look at various topology DC-DC converter and different control schemes used by DC-DC converters

- **Chapter 3** This chapter examines the working, modeling, and closed-loop control design of dual active bridge converters.

- **Chapter 4** The design of modular dual active bridge converters and the operation of a three-module ISOP dual active bridge converter are covered in this chapter.

- **Chapter 5** This chapter presents simulations and results using Plecs, MATLAB/SIMULINK, and Ltspice.

- **Chapter 6** This chapter outlines the findings from the finished work and makes recommendations for some related future research.

Chapter 2

Literature Survey

Bidirectional DC-DC converters are generally classified into two main categories: isolated and non-isolated. The primary distinction between these types lies in the presence or absence of electrical isolation. Non-isolated converters do not incorporate magnetic isolation in the power transfer process, as they operate without transformers. This results in a simpler design, reduced weight, and immunity to magnetic interference. Conversely, isolated converters first convert the input DC voltage to AC, which is then passed through a high-frequency transformer before being rectified back to DC. This configuration allows for a higher voltage gain compared to non-isolated converters, making it particularly suitable for high-power applications such as fast-charging stations [1].

This chapter provides an overview of several bidirectional DC-DC converter topologies along with a discussion on various control strategies employed to manage their operation.

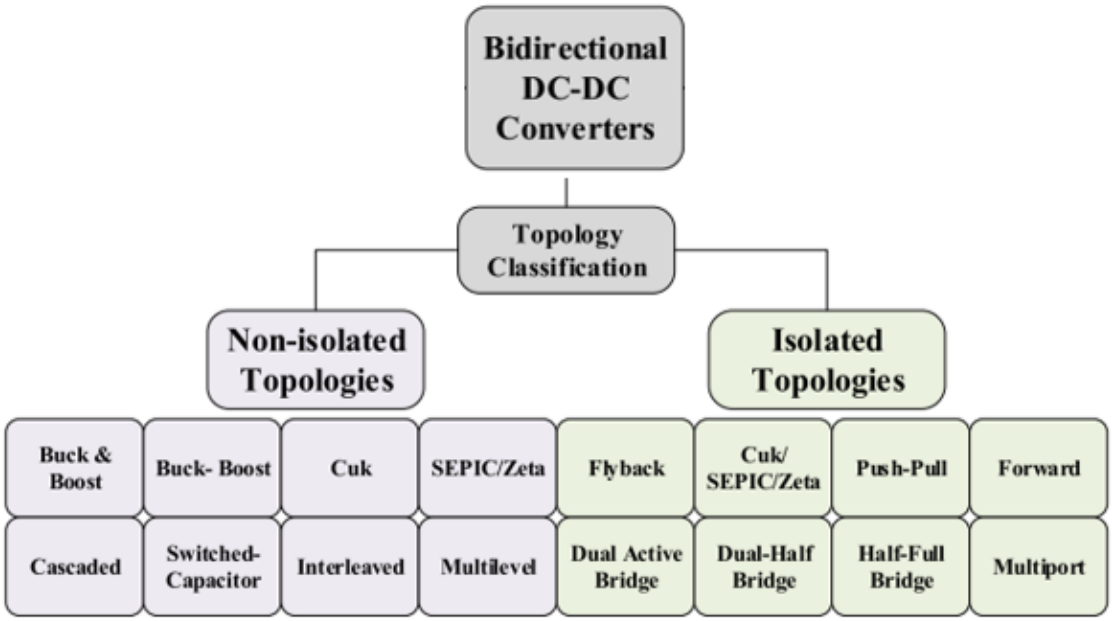

Figure 2.1: DC-DC topology converter flowchart [1]

2.1 Topology of Bidirectional DC-DC Converters

2.1.1 Isolated Converters

Currently, the most common uses for isolated bidirectional converters are in electric vehicle charging, renewable energy integration, and airplane systems. Conclusions from the completed work indicate some future work related to this one. These converters are well-suited for handling a wide range of input voltages and load conditions because of their galvanic isolation, which is achieved through transformer windings and allows for significant voltage gain due to the turns ratio [4]. Furthermore, isolation gives designers more freedom when creating a variety of input and output configurations. Isolated topologies provide improved safety for the system and linked equipment and are more suited to high-power applications than non-isolated converters.

Some of the primary isolated DC-DC converter topologies that are comparable to the Dual Active Bridge converter (which will be covered in more detail in Chapter 3)

will be briefly discussed below.

2.1.1.1 Bidirectional Flyback Converter

Also referred to as the isolated Buck-Boost bidirectional converter, this topology replaces the inductor in a conventional Buck-Boost converter with a transformer to provide galvanic isolation, as illustrated in Figure 2.2.The design of the transformer plays a critical role in the converter's performance, and a voltage clamp snubber circuit is typically included to protect against leakage currents.

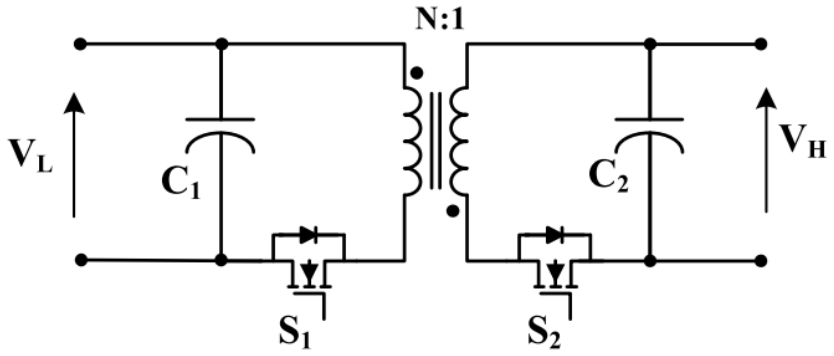

Figure 2.2: Bidirectional Flyback Converter[1]

2.1.1.2 Isolated Cuk Bidirectional Converter

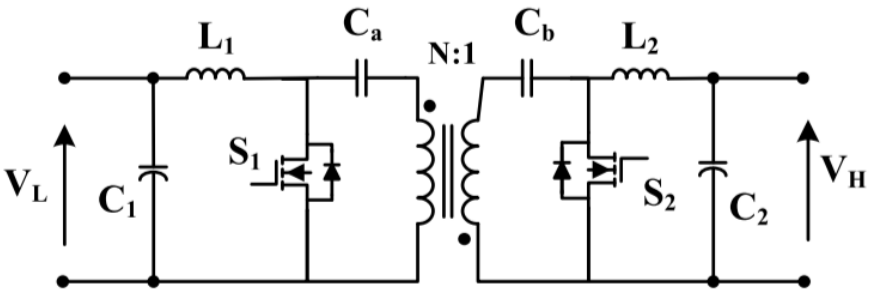

Figure 2.3: Isolated Cuk Bidirectional Converter[1]

Designed to provide the original Cuk converter the advantages of magnetic isolation. The layout of the converter, which offers isolation between the input and output sides with high voltage gain, is depicted in Figure 2.3. This converter's ability to eliminate current ripples through the coupling of the input and output inductors is a helpful feature for renewable energy systems [5].

2.1.1.3 Push-Pull Bidirectional Converter

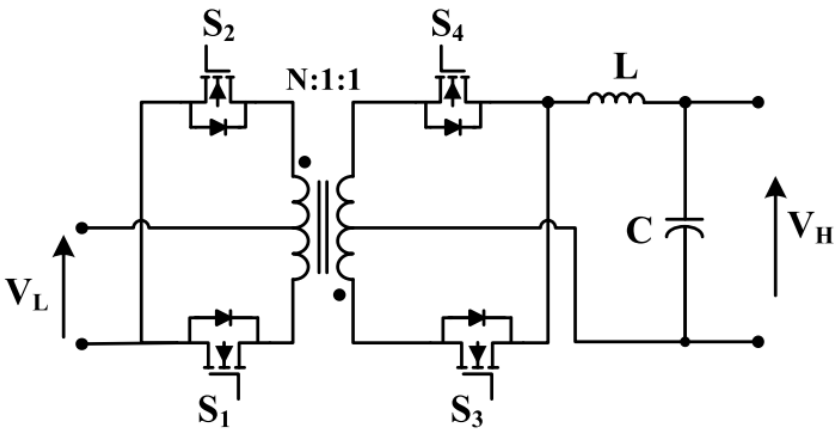

Figure 2.4: Push-Pull Bidirectional Converter[1]

The circuit illustrated in Figure 2.4 modifies the conventional push-pull converter to enable bidirectional power flow, utilizing a multi-winding transformer for energy transfer.

2.1.1.4 Bidirectional Forward Converter

A bidirectional version of the conventional forward converter is presented. By incorporating a clamping circuit, the converter achieves zero-voltage switching (ZVS). This topology also enables the development of various hybrid configurations with other isolated converter topologies.

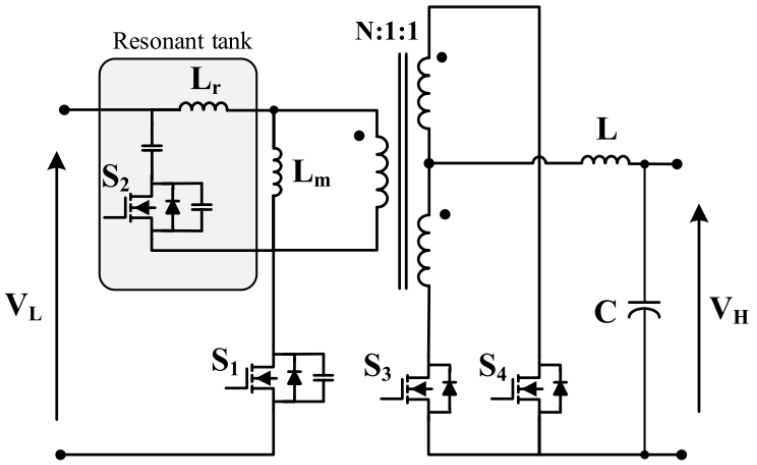

Figure 2.5: Bidirectional Forward Converter[1]

2.1.1.5 Dual Half-Bridge Converter

The Dual Half-Bridge design, depicted in Figure 2.6, is an alternative to the DAB converter. By using two voltage-fed half-bridges on each side, it can reduce the number of power switches from eight to four, making it suitable for lower-power applications. Furthermore, a current-fed architecture on the secondary side of the converter can be modified to enable a continuous current waveform.[6][7].

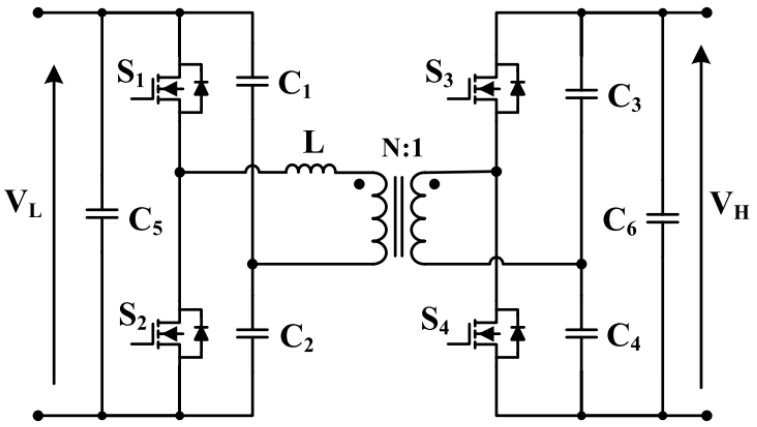

Figure 2.6: Dual Half-Bridge Bidirectional Converter[1]

2.1.1.6 Half Bridge-Full Converter

Figure 2.7 illustrates the Half Bridge–Full Bridge Converter, which consists of a voltage-fed half-bridge on the primary side and a full-bridge configuration on the secondary side. With fewer power switches than the DAB, it offers a simpler control strategy. This topology is particularly well-suited for integration in uninterruptible power supply (UPS) systems[8].

This arrangement has been modified in numerous ways, such as combining impedance networks with a full-bridge half-bridge bidirectional DC-DC converter to improve performance‘[9].

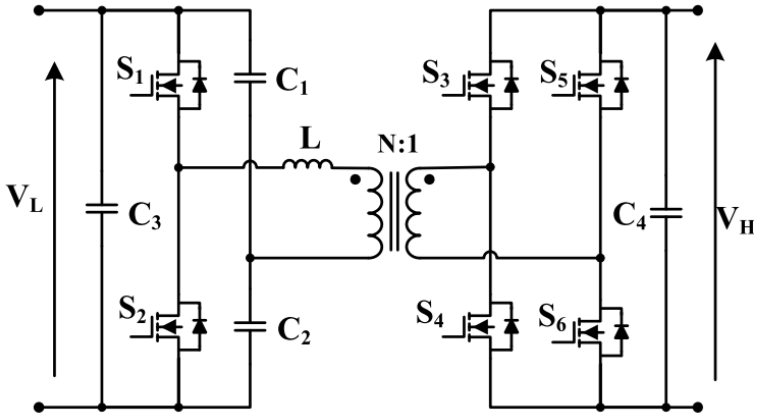

Figure 2.7: Half Full Bridge Converter[1]

2.2 Bidirectional Converter Control Schemes

Control Scheme	**Control Problems**	**Benefits**	**Limitations**
PID	- Power flow control - Minimizing switching time between two directions - Reducing dead time of switches - Protecting the elements from overcurrent	- Low cost - High reliability - High dynamic performance	- Low efficiency - Lack of robustness with uncertainties and disturbances - Weakness in avoiding large transient between directions
Sliding Mode	- Considering external perturbations in large signal - Dealing with severe variations in load and line	- Reference tracking - Fast and finite-time response - Robustness against parameter variation and external perturbation - Ability to characterise the system under small and large conditions	- Accurate parameter and state information are needed

Control Scheme	**Control Problems**	**Benefits**	**Limitations**
Fuzzy	- Minimizing power consumption from the grid - Attaining smooth performance of super-capacitor in charge/discharge - Minimizing control time	- Fast and robust response - Applicability to nonlinear and inaccurate systems	- Sensitive to expert knowledge
Digital Control	- Accurate small-signal modelling of DAB - Changing power flow directions smoothly with current protection - Improving the transient response's speed	- High EMI immunity - Enhances the efficiency and charge/discharge speed - Higher flexibility - Fault monitoring - Ease of use - Improved reliability	- Difficult to implement the electronic configuration of nonlinear control law - Requiring great analog/digital processing effort

Table 2.1: Control schemes in bidirectional converter[1]

Selecting an appropriate control strategy is crucial for achieving maximum efficiency in a converter, especially in bidirectional DC-DC applications. While various control methods are available, the most commonly adopted schemes in electric vehicle systems include PI, PID, sliding mode, fuzzy logic, and digital control.Table 2.1 benefits and limitation of the control schemes.

Chapter 3

Dual Active Bridge

The Dual Active Bridge (DAB) is a bidirectional and controllable DC-DC converter capable of handling significant power levels. Eight semiconductor switches, an energy transfer inductor, a high-frequency transformer, and DC-link capacitors are usually included. It functions similarly to a full-bridge converter when combined with a controlled rectifier.. Due to its symmetrical structure—featuring identical bridges on both the primary and secondary sides—it supports bidirectional power transfer, making it well-suited for applications such as renewable energy systems, electric vehicles (EVs), and other high-performance power conversion scenarios.

As illustrated in Figure 3.1, V_{i} and V_{o} represent the DC-link voltages, while L corresponds to the transformer's leakage inductance combined with any external energy transfer inductance. The switches S_{11-24} denote the controllable semiconductor devices. The Dual Active Bridge (DAB), widely adopted in similar applications, has traditionally employed insulated gate bipolar transistors (IGBTs) to handle high DC-link voltage requirements [10]. Typically, the switching cells S_{11-24} include anti-parallel diodes and snubber capacitors, which support current commutation during switching transitions and enable zero-voltage switching (ZVS) through the resonance between

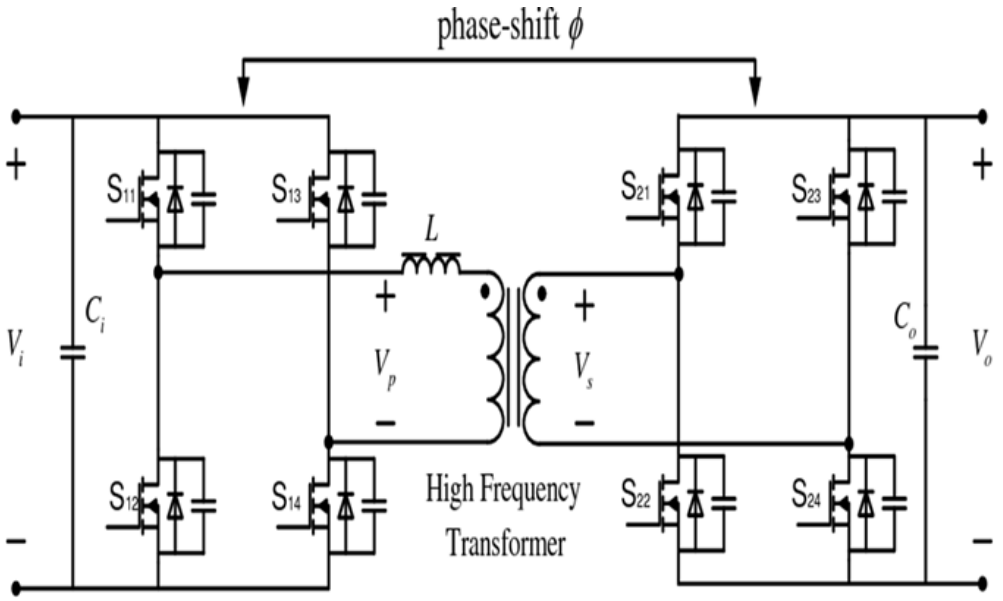

Figure 3.1: Dual Active Bridge

the snubber capacitor and the energy transfer inductance.

The motivation behind the development of high-voltage MOSFETs lies in their inherent body diode and drain-to-source output capacitance, which help eliminate the need for additional external components, thereby reducing the overall component count in the converter. Wide bandgap (WBG) materials such as silicon carbide (SiC) have gained significant attention in power electronics research due to their superior voltage and thermal handling capabilities, along with reduced turn-on energy. These characteristics make SiC devices particularly well-suited for high-frequency switching applications in modern converter designs.

3.1 Steady State Operation of DAB

A simplified electric scheme can be used to analyze a dual active bridge converter.All secondary side quantities are referred to as primary side quantities in this simplified model, which treats each half-bridge of the converter as ideal square wave

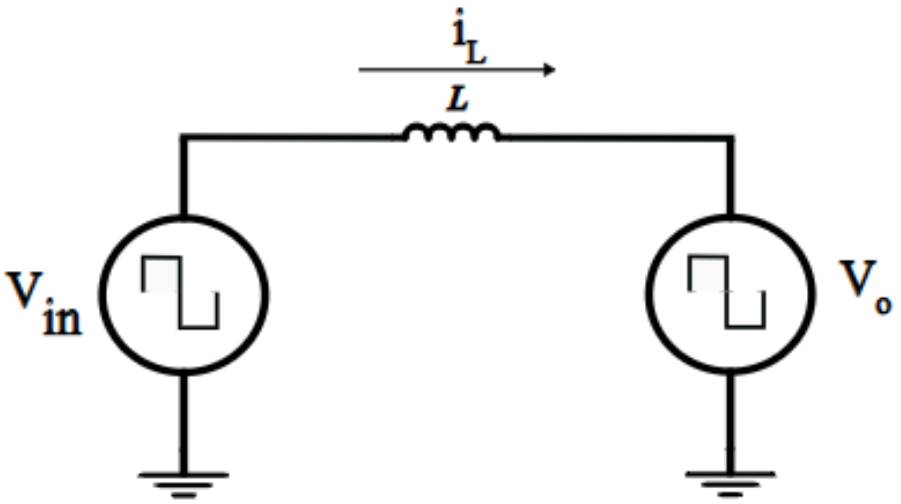

Figure 3.2: Simplified circuit of dual active bridge converter

voltage supplies on both sides. The converter generates square-wave voltage pulses at a specific frequency, referred to as the switching frequency (f_s). In applications where minimizing the size of passive components is essential, and the enhanced material characteristics of Silicon Carbide (SiC) offer significant benefits, high-frequency switching is typically implemented. At these elevated frequencies, the magnetizing inductance of the isolation transformer becomes negligible, allowing the transformer to be represented mainly by its leakage inductance. Figure 3.2 presents a simplified model of the Dual Active Bridge (DAB) converter, assuming an ideal transformer and ignoring additional parasitic elements.

The current flowing through the leakage inductance L_s, denoted as i_L, is governed by Equation 3.1. This current is considered on the primary side of the transformer [11].

$$i_L(t_1) = i_L(t_0) + \frac{1}{L_s} \int_{t_0}^{t_1} [v_{in}(t) - n \cdot v_o(t)]\, dt \tag{3.1}$$

Rewriting this expression yields Equation 3.2, which clearly shows that the slope of the current is directly proportional to the voltage difference between the two sides

and inversely proportional to the leakage inductance L_s [11].

$$\frac{di_L(t)}{dt} = \frac{v_{in}(t) - n \cdot v_o(t)}{L_s} \tag{3.2}$$

The system's average power transfer can be calculated using the current i_L, as shown in Equations 3.3a and 3.3b. Here, T_s denotes the switching period and is the reciprocal of the switching frequency f_s [11].

$$P_1 = \frac{1}{T_{S1}} \int_0^{T_{S1}} v_{in}(t) \cdot i_L(t)\, dt \tag{3.3a}$$

$$P_2 = \frac{1}{T_{S2}} \int_0^{T_{S2}} v_o(t) \cdot i_L(t)\, dt \tag{3.3b}$$

In an ideal lossless scenario, the input power equals the output power, as described in Equation 3.4a. Consequently, it can be inferred from Equation 3.4b that the secondary current $i_2(t)$ is a scaled version of the primary current, determined by the transformer turns ratio [11]. Within a lossless system, the current $i_L(t)$ not only represents the system's primary current but also corresponds to the appropriately scaled secondary current. This relationship can be described by the following equations [11]:

$$P = |P_1| = |P_2| \tag{3.4a}$$

$$n \cdot i_1(t) = i_2(t) \tag{3.4b}$$

The average power exchanged within the system depends on characteristics of the square wave, including its amplitude, frequency, duty cycle, and phase shift. Assuming that the voltage levels and physical parameters, such as the inductance L_s and the transformer turns ratio n, are maintained constant during operation, the power delivered by the dual active bridge converter and the current i_L can be controlled in the following three ways:

- By adjusting the relative phase shift ϕ, which is referred to as phase shift modulation.

- By altering one of the duty cycles, either D_1 or D_2.
- By varying the switching frequency f_s.

3.2 Switching operation in DAB

In a single-phase Dual Active Bridge (DAB) converter, both the primary and secondary full-bridge inverters are operated in a synchronized manner. Each switch within the bridges functions with a fixed duty cycle of 50%. The switches located diagonally across the bridge are switched on and off simultaneously, resulting in a square wave voltage at the output of each bridge. The detailed switching sequence of the DAB converter is discussed in the subsequent sections. For ease of analysis, the transformer is assumed to have an ideal turns ratio of $n = 1{:}1$, and its effect is neglected in the description of the switching sequence [2]. The inductor current waveform and the phase shift between the transformer's primary and secondary voltages are used to divide the switching sequence into four periods. Figure 3.9 shows the waveforms of the voltage and current.

Time interval 1: $0 < t < T_\phi \quad \left(T_\phi = \frac{\phi}{2\pi f_s} = \frac{\phi}{2\pi} T_s\right)$

During time interval 1, the inductor current exhibits both positive and negative values, indicating bidirectional flow. As a result, the current commutation pattern aligns with the sequences illustrated in Figure 3.3 and 3.4. In this period, switches Q_1 and Q_4 on the primary side, along with switches Q_6 and Q_7 on the secondary side, are responsible for conducting the current.

During this time interval, the voltage across the secondary winding, V_s, equals V_2, the voltage across the primary winding, V_p, is equal to V_1. By applying the resulting voltage difference across the leaking inductance, Equation 3.5 can be used

to approximate the rate of change of the current within this interval.

$$\frac{di}{dt} = \frac{V_1 + V_2}{L} \tag{3.5}$$

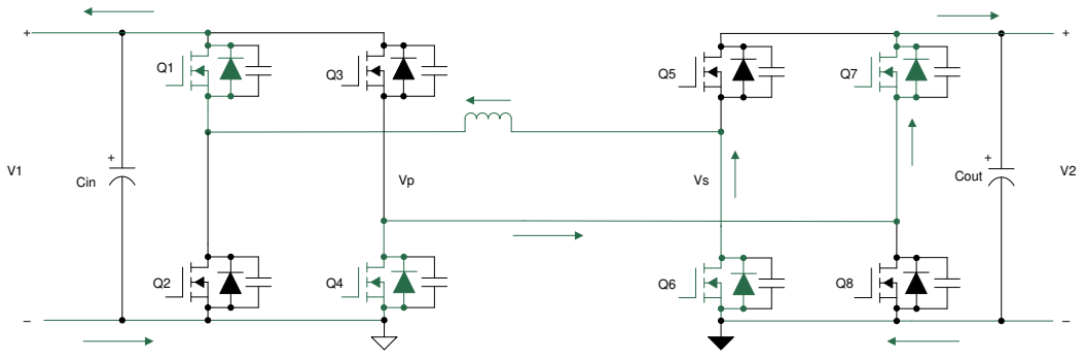

Figure 3.3: Interval 1: Negative Inductor Current[2]

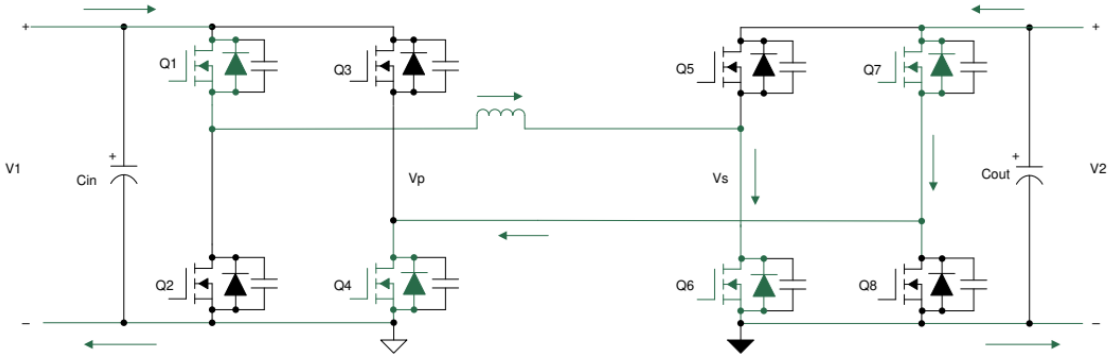

Figure 3.4: Interval 1: Positive Inductor Current[2]

Time interval 2: $T_\phi < t < \frac{T_s}{2}$

During time interval 2, the inductor current remains positive. The voltage across the primary winding of the transformer is also positive and equals V_1, while the voltage across the secondary winding is positive and equals V_2. Consequently, the voltage difference $(V_1 - V_2)$ is applied across the leakage inductor, and the slope of the increasing inductor current during this period can be determined using Equation 3.6.

$$\frac{di}{dt} = \frac{V_1 - V_2}{L} \tag{3.6}$$

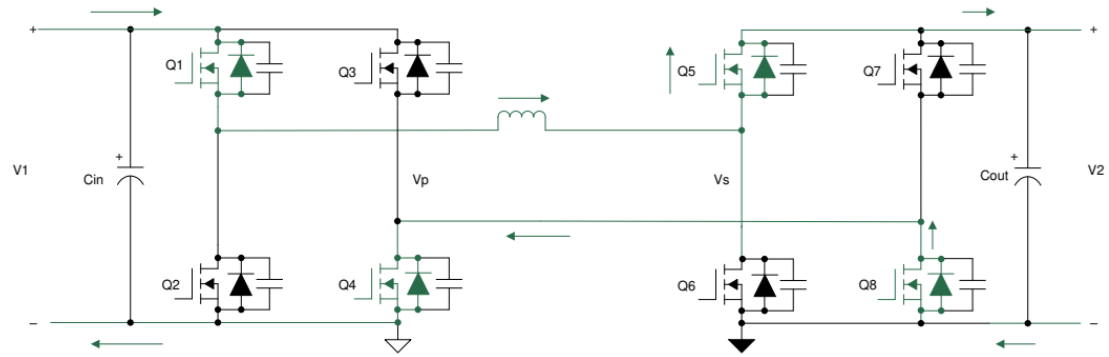

Figure 3.5: Interval 2[2]

Switches Q1 and Q4 stay on throughout this time, while switches Q5 and Q8 turn on to conduct current because the voltage across the secondary is now V2 and the inductor current is positive. Between Q6 and Q7 turning off and Q5 and Q8 turning on, there is a little dead time due to Zero voltage switching (ZVS). Figure 3.5 displays the commutation sequence for the second interval.

Time interval 3: $\frac{T_s}{2} < t < \frac{T_s}{2} + T_\phi$

In the interval 3, the inductor current begins to decrease from its positive peak toward a negative value, as illustrated in Figure 3.9. In this phase, the voltage across the transformer's primary winding becomes $-V_1$, while the voltage across the secondary remains V_2. The net voltage across the leakage inductor, given by $-(V_1 + V_2)$, results in a negative slope of the current, as described in Equation 3.7.

$$\frac{di}{dt} = -\frac{V_1 + V_2}{L} \tag{3.7}$$

Throughout this interval, switches Q5 and Q8 stay turned on. However, since the primary voltage is now $-V_1$, switches Q2 and Q3 are activated to facilitate current conduction. The bidirectional flow of the inductor current—i.e., for $I_L > 0$ and $I_L < 0$—is depicted in Figure 3.6 and Figure 3.7, respectively.

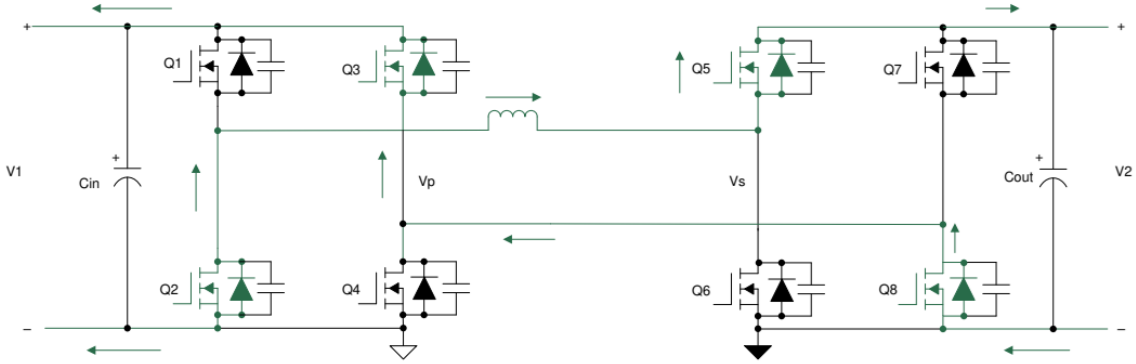

Figure 3.6: Interval 3: Positive Inductor Current[2]

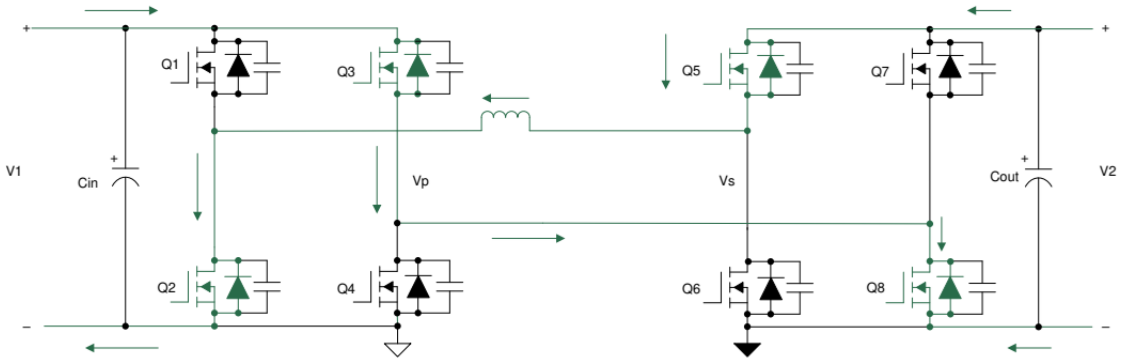

Figure 3.7: Interval 3: Negative Inductor Current[2]

Time interval 4: $\frac{T_s}{2} + T_\phi < t < T_s$

During interval 4, the inductor current remains negative. During this phase, the voltage across the primary winding is $-V_1$, and the voltage across the secondary winding is $-V_2$. As a result, the effective voltage across the leakage inductance becomes $-(V_1 - V_2)$, which leads to a negative slope in the inductor current, as expressed in Equation 3.8.

$$\frac{di}{dt} = -\frac{V_1 - V_2}{L} \tag{3.8}$$

Throughout this interval, switches Q2 and Q3 remain on. However, since the secondary voltage becomes $-V_2$, switches Q6 and Q7 are also activated to allow current conduction, as illustrated in Figure 3.8.

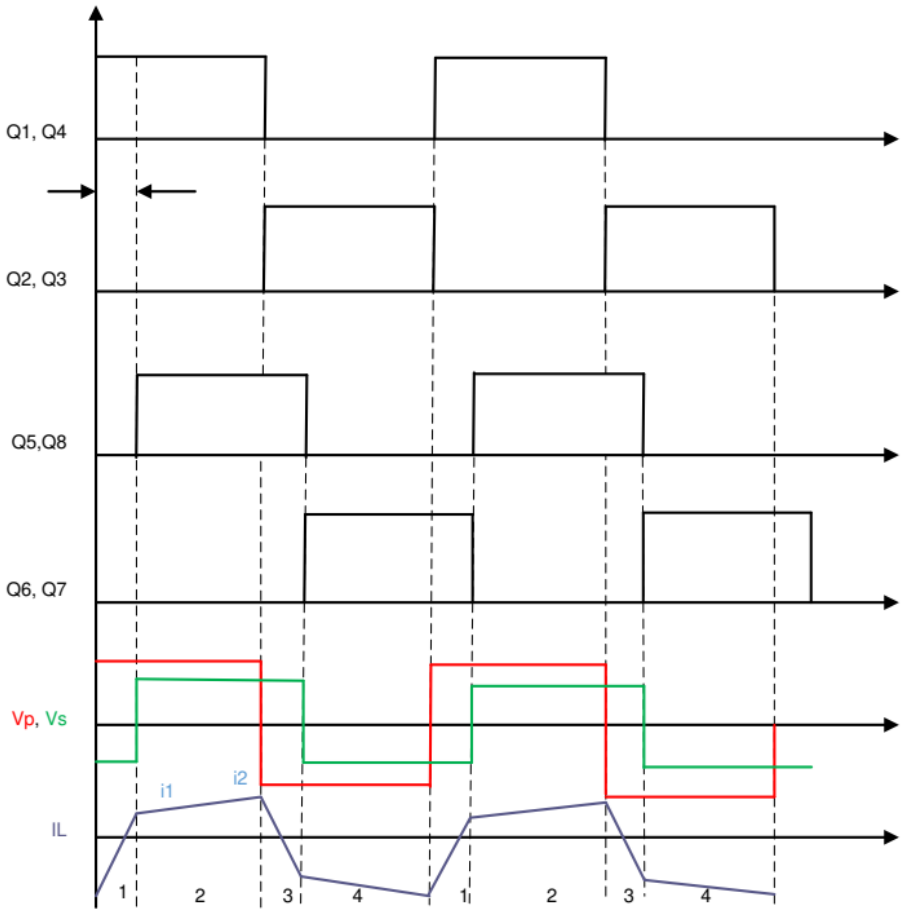

Figure 3.9: Gate Signals, Transformer Primary and Secondary Voltages, Inductor Current [2]

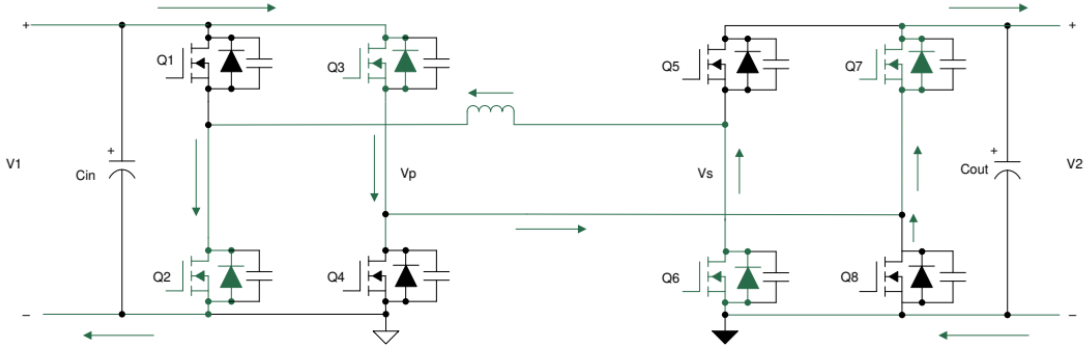

Figure 3.8: Interval 4[2]

3.3 Design Considerations for DAB

When designing a dual-active bridge's power stage, several things are crucial. The choice of leaking inductor, intended phase shift of operation, output capacitor rating, and switching frequency of operation are the most crucial elements.

3.3.1 Leakage Inductor

Being a reactive element, the inductance value is frequency-dependent. As shown in Equation 3.9, the power transfer capability of the converter can be regulated by varying the switching frequency, the energy transfer inductance, or the phase shift angle, while keeping the DC bus voltages constant.

$$L_s = \frac{nV_1V_2\phi(\pi - |\phi|)}{2\pi^2 f_s P} \tag{3.9}$$

3.3.2 Phase shift

The value leaking inductor determines the converter's phase shift. Equation 3.10 provides the phase shift needed for the necessary power transfer [2].

$$\phi = \frac{\pi}{2} \times \left(1 - \sqrt{1 - \frac{8 \times F_s \times L \times P_{\text{out}}}{N \times V_1 \times V_2}}\right) \tag{3.10}$$

3.3.3 Capacitor Selection

The proper selection of the output capacitor in a Dual Active Bridge (DAB) converter is essential for controlling voltage ripple. This component plays a significant role in determining the output voltage characteristics. The expressions in Equations (3.11) and (3.12) are derived based on the analysis shown in Figure 3.10 [11].

$$I_{\text{cap}} = I_{\text{hb2}} - I_{\text{load}} \tag{3.11}$$

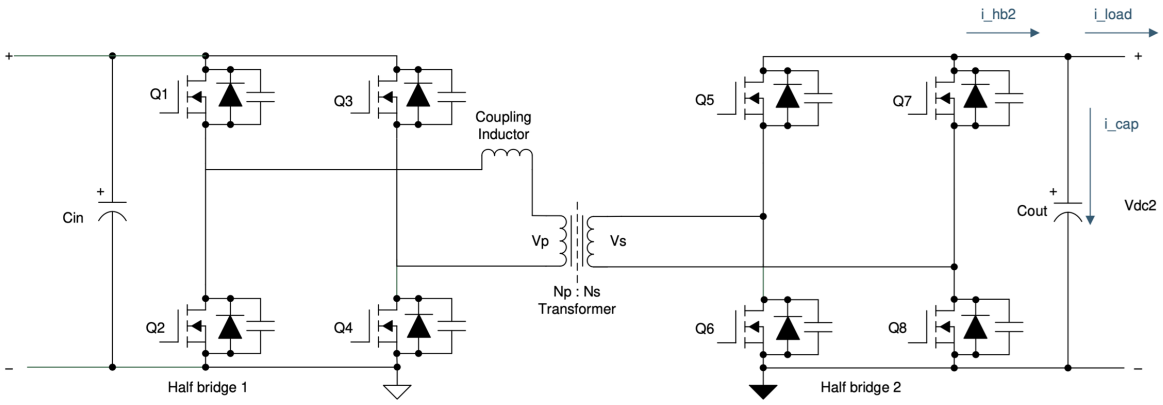

Figure 3.10: Output Capacitor Current in Dual Active Bridge [2]

Here, I_{cap} denotes the capacitor current, I_{hb2} is the output current from the second bridge, and I_{load} represents the current drawn by the load.

$$C\frac{dV_2}{dt} = \frac{V_1}{X_l}\,\phi\left(1 - \frac{\phi}{\pi}\right) - \frac{V_2}{R} \tag{3.12}$$

According to system requirements, the necessary capacitance to keep voltage ripple within predetermined bounds for a given phase shift and inductance rises as the leakage inductor value grows. Therefore, in order to properly handle the voltage ripple, greater capacitance is required. The dissipation of losses across the capacitor's equivalent series resistance (ESR) increases as the RMS value of the current increases. These factors are taken into account while choosing the output capacitor, which keeps the output voltage under a 5% ripple [2].

3.3.4 Switching Frequency

Another important design parameter that significantly impacts both the efficiency and power density of a power converter is the switching frequency. The choice of switching devices in the power stage primarily depends on the input and output voltage levels. The integration of SiC MOSFETs in the power stage allows for operation at notably high switching frequencies. In this design, the switching frequency is set to

$f_{\text{sw}} = 100\,\text{kHz}$.

3.3.5 Transformer selection

Transformers and inductors are key components that significantly influence the physical dimensions of a power supply. Operating at higher switching frequencies can lead to a reduction in the size of these magnetic components. However, beyond a certain threshold, increasing the switching frequency adversely affects the efficiency of the power converter. This degradation is primarily due to the skin effect, wherein the current tends to flow near the surface of the conductor at elevated frequencies. Additionally, the proximity effect causes current to concentrate on the adjacent surfaces of closely spaced conductors. Consequently, in high-frequency designs, careful optimization of conductor dimensions and layer configurations is necessary to mitigate proximity-related losses [2].

To address these challenges, planar transformers were selected for this design due to their numerous advantages over traditional wound transformers:

- Planar magnetics offer a significantly higher power density, occupying less physical space while maintaining the same power handling capability.
- They support extensive interleaving, which effectively reduces AC conduction losses.
- Uniform spacing between turns and layers enables accurate and consistent values of leakage inductance and intra-winding capacitance.
- Precise control over leakage inductance is achievable with planar construction techniques.

- Their compact form factor allows the integration of a shim inductor within the transformer structure, eliminating the need for a separate board-mounted component.

While the leakage inductance plays a critical role in enabling soft switching up to a certain load level, it alone is insufficient to guarantee soft switching under light-load conditions. Typically, the leakage inductance is designed to support soft switching up to half or one-third of the rated load. To extend soft switching capabilities to near-zero load conditions, the magnetizing inductance of the transformer—usually chosen to be approximately ten times the leakage inductance—is utilized to maintain soft switching behavior at light loads.

3.4 Converter Modelling

Modeling the dynamics of the Dual Active Bridge (DAB) converter has been extensively explored in recent literature [12], with particular emphasis on accurately deriving the converter's transfer functions. A noteworthy approach utilizes the Fourier series expansion of the switching functions, which has shown effectiveness in modeling the DAB's behavior over a wide power range.

As presented in [12], the input and output voltages are first defined using the switching states and the corresponding primary and secondary side voltages in this modeling technique.:

$$V_1 = V_i(S_1 - S_2) \tag{3.13}$$

$$V_2 = V_o(S_5 - S_6) \tag{3.14}$$

To complete the model, a current-based expression for the output voltage is necessary. This requires applying Kirchhoff's Current Law (KCL) at the converter's output node. Here, the output bridge current i_{DC} and the capacitor current i_c must balance the load current i_{out}, yielding the relation:

$$i_c = i_{DC} - i_{out} \tag{3.15}$$

The switching states of the output bridge determine the value of i_{DC}, as shown in Table 3.1.

Table 3.1: Output Bridge Switching States

S_5	S_6	i_{DC}
0	0	0
0	1	$-i_L$
1	0	i_L
1	1	0

The current injected by the output bridge can be defined as:

$$i_{DC} = i_L(S_5 - S_6) \tag{3.16}$$

To fully describe the system dynamics, a closed-loop Kirchhoff's Voltage Law (KVL) equation must be formulated for the inner loop that includes the inductor current, load resistance, and corresponding bridge voltages. This results in the following expression:

$$V_p - \frac{N_p}{N_s}V_s - R_L i_L - L\frac{di_L}{dt} = 0 \tag{3.17}$$

Substituting equations (3.13) and (3.14) into equation (3.17), we arrive at the final voltage equation in terms of the switching states and inductor current:

$$R_L i_L + L\frac{di_L}{dt} = V_i(S_1 - S_2) - \frac{N_p}{N_s}V_o(S_5 - S_6) \tag{3.18}$$

To express the switching functions S_1, S_2, S_5, and S_6 in the time domain, they can be expanded using a Fourier series. Since these functions are square waveforms, their expansion is given by:

$$S_k = \frac{1}{2} + \frac{2}{\pi}\sum_{n=0}^{N}\frac{\sin\left([2n+1](\omega_s t - \alpha_k)\right)}{2n+1}, \quad N \geq 0, \quad k = 1, 2, 3, ... \tag{3.19}$$

Here, N denotes the number of harmonics considered in the expansion, and α_k represents the phase shift of the k-th switching function. Including more harmonics improves the accuracy of the reconstructed waveform, closely approximating the original square wave signal. Applying the previously derived Fourier series expansion of the switching functions to the MOSFETs relevant to the DAB operation yields the following expressions:

$$S_1 = \frac{1}{2} + \frac{2}{\pi}\sum_{n=0}^{N}\frac{\sin\left([2n+1]\omega_s t\right)}{2n+1}, \quad N \geq 0, \quad k = 1, 2, 3, \ldots \tag{3.20a}$$

$$S_2 = \frac{1}{2} + \frac{2}{\pi}\sum_{n=0}^{N}\frac{\sin\left([2n+1](\omega_s t - \pi)\right)}{2n+1}, \quad N \geq 0, \quad k = 1, 2, 3, \ldots \tag{3.20b}$$

$$S_5 = \frac{1}{2} + \frac{2}{\pi}\sum_{n=0}^{N}\frac{\sin\left([2n+1](\omega_s t - \delta)\right)}{2n+1}, \quad N \geq 0, \quad k = 1, 2, 3, \ldots \tag{3.20c}$$

$$S_6 = \frac{1}{2} + \frac{2}{\pi}\sum_{n=0}^{N}\frac{\sin\left([2n+1](\omega_s t - \delta - \pi)\right)}{2n+1}, \quad N \geq 0, \quad k = 1, 2, 3, \ldots \tag{3.20d}$$

These expressions represent the time-domain behavior of the square-wave switching functions used in the DAB's MOSFETs. The variable ω_s denotes the switching angular frequency, while δ corresponds to the applied phase shift.

The foundational analysis discussed above, based on the Fourier representation of switching waveforms, is utilized in [12] to derive a standard form of the DAB's transfer function. By appropriately recombining and rearranging these expressions, the complete nonlinear model of the converter can be obtained. The dynamic behavior of the output voltage can be expressed as a nonlinear function of the output voltage V_{out} and the phase shift δ, incorporating the effect of the load current i_{load}:

$$\frac{dV_{out}}{dt} = f(V_{out}, \delta) = -i_{load} + \frac{8}{C_{out}\pi^2}\frac{N_p}{N_s}\sum_{n=0}^{N}\frac{1}{[2n+1]^2}\left(\frac{V_i}{|Z[n]|}\cos\left((2n+1)\delta - \varphi_z[n]\right)\right. \\ \left. - \frac{N_p}{N_s}\frac{V_o}{|Z[n]|}\cos(\varphi_z[n])\right) \tag{3.21}$$

Where:

$$Z[n] = \sqrt{R_L^2 + (2\pi f_s[2n+1]L)^2}, \quad \varphi_z[n] = \tan^{-1}\left(\frac{2\pi f_s[2n+1]L}{R_L}\right)$$

To enable small-signal analysis, the nonlinear equation is linearized around an operating point using a first-order Taylor series expansion:

$$\frac{d(V_{out} + \Delta V_{out})}{dt} \approx f(V_{out0}, \delta_0, i_{load0}) + \left.\frac{\partial f}{\partial V_{out}}\right|_0 \Delta V_{out} + \left.\frac{\partial f}{\partial i_{load}}\right|_0 \Delta i_{load} + \left.\frac{\partial f}{\partial \delta}\right|_0 \Delta\delta \tag{3.22}$$

Rearranging the terms, the final linearized differential equation for the output voltage is given in standard first-order form as:

$$\frac{d\Delta V_{out}}{dt} = A\Delta V_{out} + B_\delta \Delta\delta + B_I \Delta i_{load} \tag{3.23a}$$

$$A = \frac{-8}{C_{out}\pi^2}\left(\frac{N_p}{N_s}\right)^2 \sum_{n=0}^{N}\frac{\cos(\varphi_z[n])}{[2n+1]^2|Z[n]|} \tag{3.23b}$$

$$B_\delta = \frac{-8}{C_{out}\pi^2}\frac{N_p}{N_s}\sum_{n=0}^{N}\frac{\sin\left(\varphi_z[n] - [2n+1]\delta_0\right)}{[2n+1]|Z[n]|} \tag{3.23c}$$

$$B_I = -\frac{1}{C_{out}} \tag{3.23d}$$

These expressions characterize the small-signal behavior of the converter, allowing for control design and system stability analysis.

3.5 Controller Design

Figure 3.11 shows the typical feedback control architecture of a power converter. The plant or converter model is represented by $G(s)$ in this setup, the controller is indicated by $C(s)$, the measured output voltage is V_{out}, and the reference signal that the system seeks to follow is V_{ref}. The main controllable variable in this loop is the output voltage.[13].

An error signal is produced in closed-loop operation by periodically sampling the output and comparing it to the reference signal. After processing this error, the controller provides the plant with the proper control input. This control loop aims to achieve zero steady-state error by minimizing the difference between the output and reference signals. This technique keeps the system regulated against disruptions and guarantees that it reacts precisely to changes in the reference.

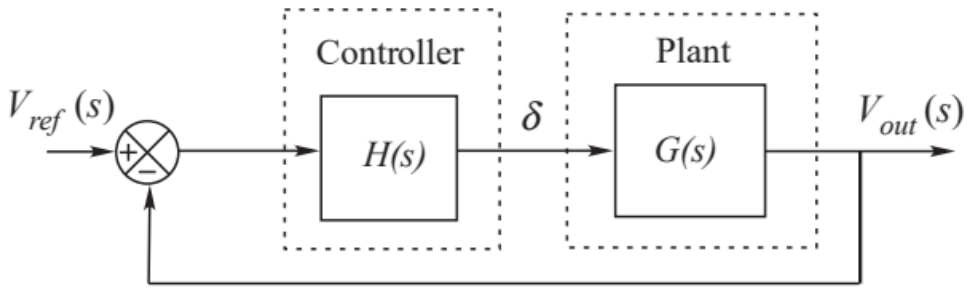

Figure 3.11: Standard feedback control loop system.

Based on the system model derived in the previous, a corresponding plant transfer function can be formulated. This is achieved by converting the time-domain system equations into the Laplace domain. For simplification, the effect of load current distur-

bances is neglected, which allows for a more straightforward design of a steady-state tracking controller.

Applying the Laplace transform to the linearized equation in (38) and rearranging yields the plant transfer function:

$$G(s) = \frac{B_\delta}{s - A} \tag{3.24}$$

Since the plant model is of first-order, a proportional-integral (PI) controller is well-suited for implementation. The PI controller ensures zero steady-state error and is widely adopted for such applications [14][15]. The transfer function of the PI controller is given by:

$$C(s) = G(s) = K_p + \frac{K_i}{s} \tag{3.25}$$

where K_p is the proportional gain and K_i is the integral gain.

With both the plant and controller transfer functions established, the overall closed-loop input-output transfer function can be expressed as:

$$F(s) = C(s)G(s) = \left(K_p + \frac{K_i}{s}\right)\left(\frac{B_\delta}{s - A}\right) \tag{3.26}$$

Chapter 4

Modular Architecture of DAB

In DC-DC converters, the power stage is divided into several smaller converter units that run in parallel as part of the modular architecture. This architecture improves fault tolerance, scalability, and thermal management. The architecture enhances dynamic response and minimizes output ripple by interleaving module operations. It also makes maintenance easier and allows for flexible power scaling, which makes it perfect for applications like data centers, electric cars, and aerospace systems.

In modular DC-DC converters, the Input-Series Output-Parallel (ISOP) topology is widely used, particularly for applications requiring high voltage and high current. In order to handle greater input voltages, this structure connects several converter modules in series at the input. It also connects their outputs in parallel to provide higher load current. This setup guarantees current sharing at the output and voltage sharing among modules at the input. Improved efficiency, less voltage stress on individual switches, and better use of power components are just a few advantages that ISOP provides. Because each module can be separately regulated and dynamically balanced using the right control techniques, it also improves fault tolerance and dependability.

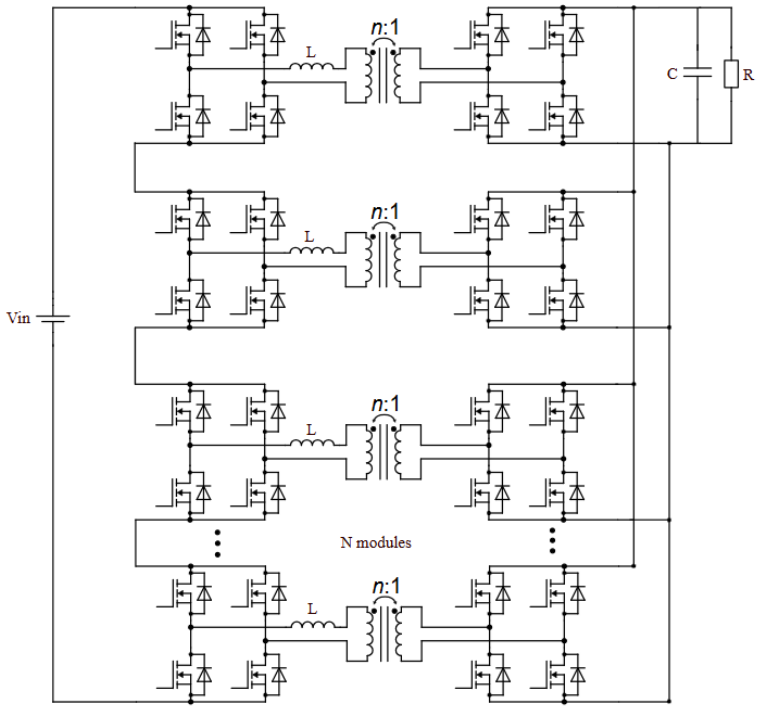

Figure 4.1: N module DAB

4.1 Modelling of Input Series Output Parallel(ISOP) DAB

In this section our main goal is to construct a power converter that can handle higher input voltage and higher output power by analyzing the input-series output-parallel (ISOP) connection of DAB converters. From the perspective of the converters' operation in an ISOP connection, the controller must ensure that all modules operate properly and that the converters share power appropriately, while maintaining crucial features like soft switching. The modules' consistent input voltage distribution allows for this balanced operation.[3].

A converter architecture with N DAB modules in ISOP connection is shown in figure 4.1.

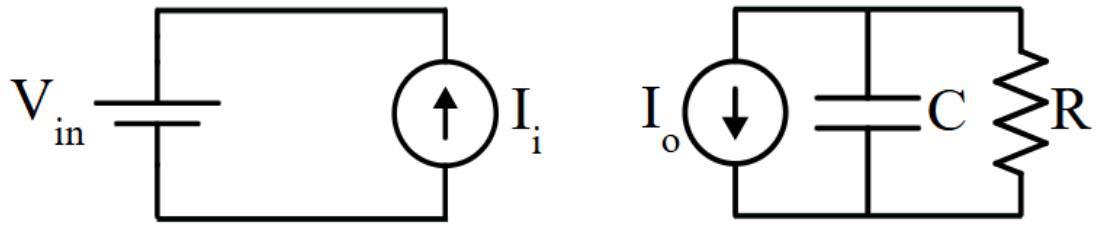

Figure 4.2: Average model of a DAB Converter

4.1.1 Average Model of DAB

The average model of the converter can be represented by two current sources 4.2, one for the input current and another one for the output current. The equations of the average model of an ideal DAB converters 4.1, 4.2, and 4.3 are presented in [16].The average output current I_o and average input current I_i of the converter can be expressed in terms of the circuit parameters and control variables. Here, T is half the switching period, D denotes the normalized phase shift (i.e., the duty cycle), n is the transformer turns ratio, and L_k represents the leakage inductance of the transformer. The variables V_in and V_o are the input and average output voltages, respectively, while R is the resistive load.

The corresponding expressions for average output current, input current, and output voltage are given by:

$$I_o = \frac{T \cdot V_\mathrm{in} \cdot D \cdot (1 - D)}{L_k \cdot n} \tag{4.1}$$

$$I_\mathrm{in} = \frac{T \cdot V_o \cdot D \cdot (1 - D)}{L_k \cdot n} \tag{4.2}$$

$$V_o = \frac{T \cdot V_\mathrm{in} \cdot D \cdot (1 - D)}{L_k \cdot n} \cdot R \tag{4.3}$$

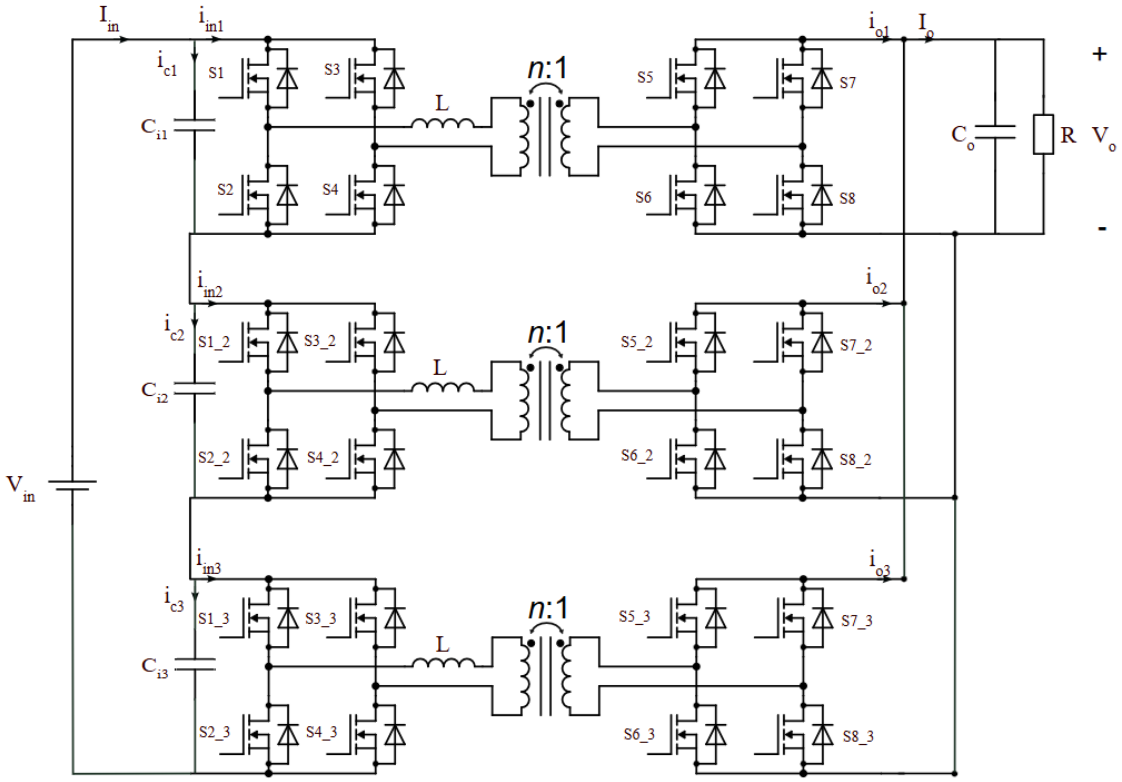

Figure 4.3: DAB converters in input series output parallel connection

Equation 4.2 shows that the output voltage and input current of a Dual Active Bridge (DAB) converter are influenced by the switching period T, phase shift ratio D, leakage inductance L_k, and transformer turns ratio n. In an Input-Series Output-Parallel (ISOP) configuration, all modules ideally share the same output voltage and input current, as illustrated in Figure 4.3. However, if the modules are not perfectly identical and operate with the same phase shift D and switching period T, discrepancies arise between the total input current I_{in} (defined by the series connection) and the individual input currents of each module ($i_{\text{in1}}, i_{\text{in2}}, i_{\text{in3}}$). These mismatches cause non-zero currents to flow through the input capacitors, initiating a self-reinforcing imbalance in which a single module may eventually bear the entire input voltage, leading to instability in the system [3].

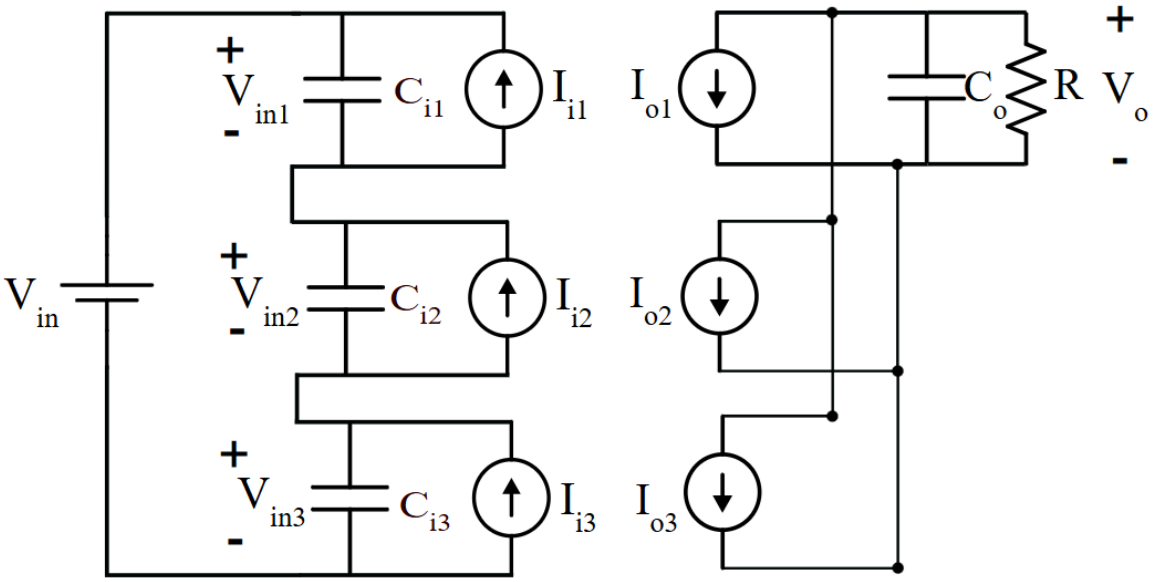

Figure 4.4: Average model of DAB converter in ISOP configuration

4.1.2 Modelling DAB in ISOP Connection

Perturbing the equations of the average model as shown in previous section, the value of the dependent current sources in the ISOP connection model gives the following equation (Fig 4.4) [3] :

$$\hat{i}_{oj} = g_{od} \cdot \hat{d}_j + g_{ovi} \cdot \hat{v}_{ij} \tag{4.4}$$

$$\hat{i}_{ij} = g_{id} \cdot \hat{d}_j + g_{ivo} \cdot \hat{v}_o \tag{4.5}$$

Where

$$g_{od} = \frac{V_i \cdot T(1-2\cdot D)}{3 \cdot L_k \cdot n} \tag{4.6}$$

$$g_{id} = \frac{V_o \cdot T(1-2\cdot D)}{L_k \cdot n} \tag{4.7}$$

$$g_{ovi} = g_{ivo} = \frac{T \cdot D \cdot (1-D)}{L_k \cdot n} \tag{4.8}$$

The following assumptions are made for the modeling of the system [17]:

- All converter modules share identical parameters, including the leakage inductance L_k, transformer turns ratio n, switching period T, and input capacitor values, such that $C_{i1} = C_{i2} = C_{i3} = C_i$.
- Each module receives an equal share of the total input voltage, with the DC input voltages defined as $V_{i1} = V_{i2} = V_{i3} = \frac{V_{in}}{3}$.
- The modules operate with the same nominal time shift, i.e., $D_1 = D_2 = D_3 = D$, at the operating point. However, variations due to perturbations are considered, such that $\hat{d}_1 \neq \hat{d}_2 \neq \hat{d}_3$.

The fundamental equations describing this model are presented in Equations (4.9) and (4.10), which relate the perturbations in the input voltage of each module and the perturbation in the output voltage to the variations in their respective duty cycles. The coefficients g_{od} and g_{id} are derived from Equations (4.6) and (4.7). Here, V_{in} represents the total input voltage, and V_o denotes the output voltage [17].

$$\hat{v}_{inj} = \frac{1}{C_i \cdot s} \cdot g_{id} \cdot \left(\frac{1}{3} \cdot (\hat{d}_1 + \hat{d}_2 + \hat{d}_3) - \hat{d}_j \right) \tag{4.9}$$

$$\hat{v}_o = \frac{R}{RC_o s + 1} \cdot \frac{g_{od}}{3} \cdot (\hat{d}_1 + \hat{d}_2 + \hat{d}_3) = G_{vd}(s) \cdot (\hat{d}_1 + \hat{d}_2 + \hat{d}_3) \tag{4.10}$$

4.1.3 Decoupling of Control Loops

Several approaches can be taken into consideration in order to attain a uniform distribution of input voltages. Using one control loop for the input voltages and another for the output voltage is one method. Only N-1 input voltages need to be regulated when N modules are involved. Only three modules are taken into account in the computations here for simplicity's sake. It is simple to expand the described process to include more converters. In the previous section, a small-signal model of

the three DAB modules connected in an ISOP configuration was derived [3]. This model captures the relationship between the duty cycle perturbations and the resulting variations in input and output voltages. The complete model is expressed asin Equations (4.11) and (4.12):

$$\begin{bmatrix} \hat{v}_{i1} \\ \hat{v}_{i2} \\ \hat{v}_o \end{bmatrix} = \underbrace{\begin{bmatrix} -2A(s) & A(s) & A(s) \\ A(s) & -2A(s) & A(s) \\ G_{vd}(s) & G_{vd}(s) & G_{vd}(s) \end{bmatrix}}_{H(s)} \begin{bmatrix} \hat{d}_1 \\ \hat{d}_2 \\ \hat{d}_3 \end{bmatrix} \tag{4.11}$$

Here, the function $A(s)$ is defined as:

$$A(s) = \frac{g_{id}}{3C_i s} = \frac{1}{3C_i s L_k n} \cdot T \cdot V_o(1 - 2D) \tag{4.12}$$

The modular converter operates as a Multiple-Input Multiple-Output (MIMO) system, where strong interdependencies exist between the control signals and the controlled variables. As a result, traditional Single-Input Single-Output (SISO) control techniques are not directly applicable to this configuration. However, by implementing the control strategy proposed in [18], the system can be restructured to behave as three decoupled SISO subsystems, thus enabling the application of simpler control methodologies.

If we can diagonalize the matrix H(s) (4.11) then only one controlled quantity will be affected by each control signal, and only one control signal will be dependent on each control quantity..Decomposing the original matrix H(s) as the product of two matrices, one of which is diagonal, is the way to go. For this specific instance, a diagonal matrix D(s) is suggested in (4.13). Keep in mind that every diagonal element of D(s) is a common factor of the matching row of the matrix H(s) in equation (4.11).

$$H(s) = D(s) \cdot Y(s) = \begin{bmatrix} 3A(s) & 0 & 0 \\ 0 & 3A(s) & 0 \\ 0 & 0 & 3G_{vd}(s) \end{bmatrix} \cdot Y(s) \tag{4.13}$$

Applying Equation (4.13) to the system in Equation (4.11), the transformed system becomes:

$$\begin{bmatrix} \hat{v}_{i1} \\ \hat{v}_{i2} \\ \hat{v}_o \end{bmatrix} = \begin{bmatrix} 3A(s) & 0 & 0 \\ 0 & 3A(s) & 0 \\ 0 & 0 & 3G_{vd}(s) \end{bmatrix} \cdot Y(s) \begin{bmatrix} \hat{d}_1 \\ \hat{d}_2 \\ \hat{d}_3 \end{bmatrix} = \begin{bmatrix} 3A(s) & 0 & 0 \\ 0 & 3A(s) & 0 \\ 0 & 0 & 3G_{vd}(s) \end{bmatrix} \begin{bmatrix} \hat{x}_1 \\ \hat{x}_2 \\ \hat{x}_3 \end{bmatrix} \tag{4.14}$$

A new set of control variables, denoted as (x_1, x_2, x_3), is introduced to satisfy the condition presented in Equation (4.15).

$$Y(s) \begin{bmatrix} \hat{d}_1 \\ \hat{d}_2 \\ \hat{d}_3 \end{bmatrix} = \begin{bmatrix} \hat{x}_1 \\ \hat{x}_2 \\ \hat{x}_3 \end{bmatrix} \tag{4.15}$$

In the transformed system described by Equation (4.14), the controlled outputs are expressed in terms of the newly defined control inputs x_j. This transformation enables the decomposition of the MIMO system into three decoupled Single-Input Single-Output (SISO) systems. Each output variable is now influenced by only one corresponding control signal, and each control signal exclusively affects one output. As a result, individual compensators can be independently designed for each SISO loop. These compensators will be responsible for generating the required control variables x_j.

The transformation matrix $Y(s)$ is defined as the product of the inverse of $D(s)$ and $H(s)$, as shown in Equation (4.16):

$$Y(s) = D(s)^{-1} \cdot H(s) = \begin{bmatrix} -\frac{2}{3} & \frac{1}{3} & \frac{1}{3} \\ \frac{1}{3} & -\frac{2}{3} & \frac{1}{3} \\ \frac{1}{3} & \frac{1}{3} & \frac{1}{3} \end{bmatrix} \tag{4.16}$$

As a result, the normalized time shifts d_j can be readily computed from the newly defined control variables x_j, as shown in Equation (4.17). Since $Y(s)$ is a constant matrix with full rank, its inverse exists and can be used directly. It is important to note that in practical implementations of the control strategy for DAB converters, the actual control inputs are the normalized time shifts d_j.

$$\begin{bmatrix} \hat{d}_1 \\ \hat{d}_2 \\ \hat{d}_3 \end{bmatrix} = Y(s)^{-1} \cdot \begin{bmatrix} \hat{x}_1 \\ \hat{x}_2 \\ \hat{x}_3 \end{bmatrix} = \begin{bmatrix} -\hat{x}_1 + \hat{x}_3 \\ -\hat{x}_2 + \hat{x}_3 \\ \hat{x}_1 + \hat{x}_2 + \hat{x}_3 \end{bmatrix} \tag{4.17}$$

Figure 4.5 shows the block diagram of the modular converter system based on the recently created control variables (x_1, x_2, x_3). The compensators C_1, C_2, and C_3 are designed using this schematic as a basis. Additionally, it permits the inclusion of modulator gains and sensor dynamics, however for simplicity's sake, these are taken to be equal to one in the figure. Figure 4.6 shows how the controller is actually put into practice. The auxiliary control variables x_1, x_2, and x_3, which correlate to the outputs of the corresponding compensators, are used in this setup to determine the actual control signals applied to the converter.

An ideal model of the converter modules was assumed to facilitate the decoupling methodology. Nevertheless, this method can also be extended to practical converters (e.g., those characterized by measured frequency responses), provided the following two conditions are fulfilled [17]:

Condition 1: The output voltage must exhibit an identical dependency on each of the duty cycles d_j. For three converter modules, this requirement can be represented as:

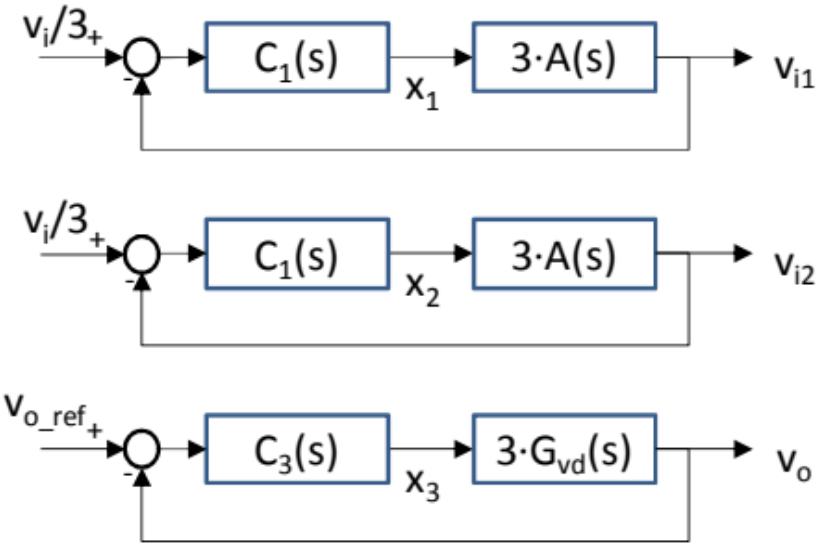

Figure 4.5: Output voltage and Input voltage control loops for compensator value calculations[3]

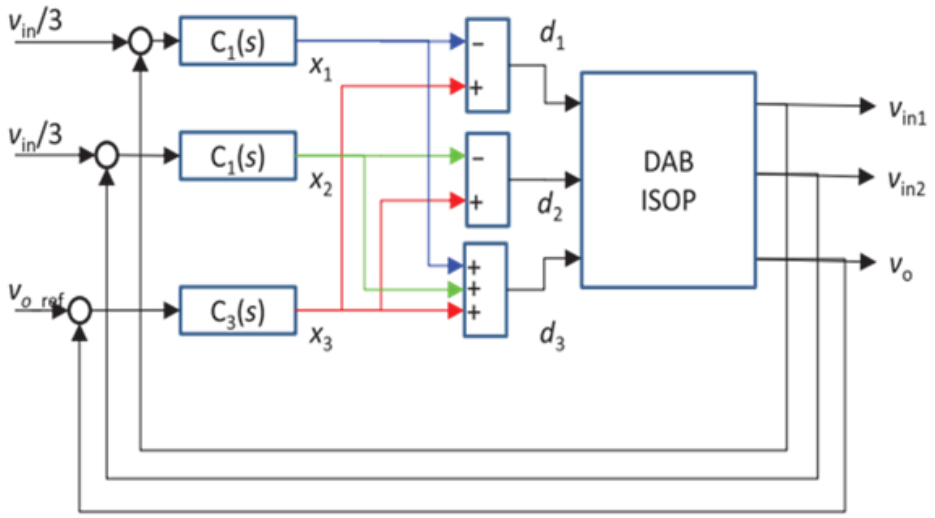

Figure 4.6: Decoupled loops control scheme implementation[3]

$$\left.\frac{\hat{v}_o}{\hat{d}_1}\right|_{\hat{d}_2=0,\,\hat{d}_3=0} = \left.\frac{\hat{v}_o}{\hat{d}_2}\right|_{\hat{d}_1=0,\,\hat{d}_3=0} = \left.\frac{\hat{v}_o}{\hat{d}_3}\right|_{\hat{d}_1=0,\,\hat{d}_2=0} \tag{15}$$

Condition 2: The input voltage transfer function of each module with respect to its own duty cycle must be proportional to its input voltage transfer function with respect to the duty cycles of the other modules. This condition, applied to three modules, can be written as:

$$\left.\frac{\hat{v}_{\text{in1}}}{\hat{d}_1}\right|_{\hat{d}_2=0,\,\hat{d}_3=0} = M \cdot \left.\frac{\hat{v}_{\text{in1}}}{\hat{d}_2}\right|_{\hat{d}_1=0,\,\hat{d}_3=0} = M \cdot \left.\frac{\hat{v}_{\text{in1}}}{\hat{d}_3}\right|_{\hat{d}_1=0,\,\hat{d}_2=0} \tag{16}$$

Here, M is a constant that characterizes the proportionality. In the case under consideration, $M = -\frac{1}{2}$.

Chapter 5

Simulation and Results

5.1 DAB closed loop simulation

The simulation is carried out in the PLECS platform, and the electrical and control parameters of DAB converter are shown in Table 5.1. As demonstrated in this thesis's

Table 5.1: Converter Parameters

Parameters	**Symbol**	**Value**
Power rating	P	10kW
Input Voltage	V_{in}	750 V
Output Voltage range	V_o	300-500 V
Leakage Inductance	L	0.0102 mH
Parasitic Resistance	R	$200m\Omega$
Switching Frequency	f_s	100 kHz
Transformer Ratio	n	0.5
Output Capacitance	C	660 μF
Load Resistance	R	10Ω, 10Ω

third chapter, the closed loop control was created appropriately. There are two models in the figure 5.1, 5.2: The plecs model and the phase shift control model.

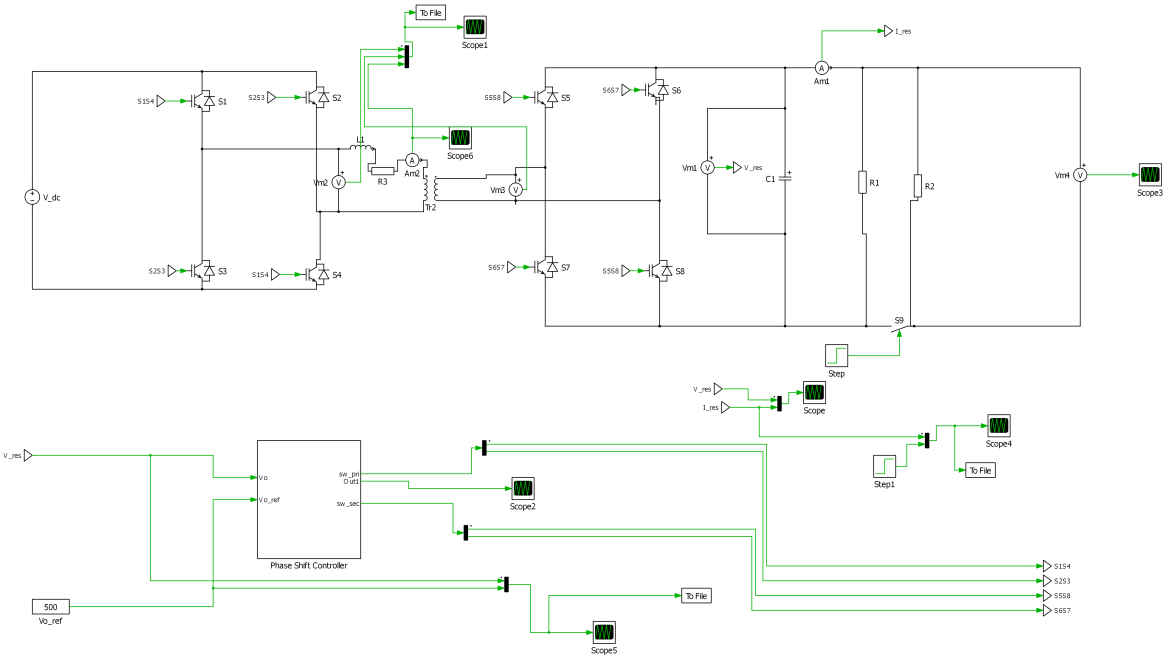

Figure 5.1: Plecs simulation model of DAB

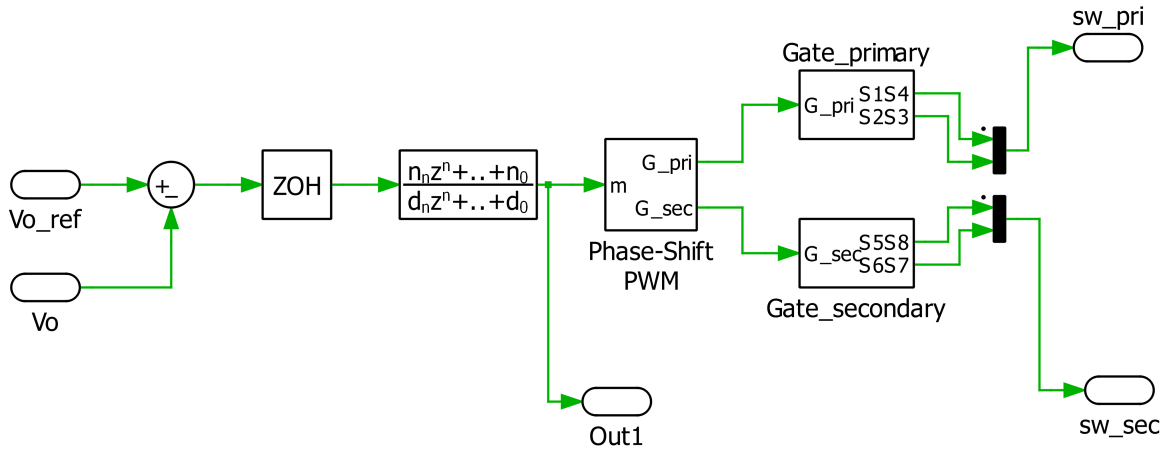

Figure 5.2: Phase Shift control of DAB

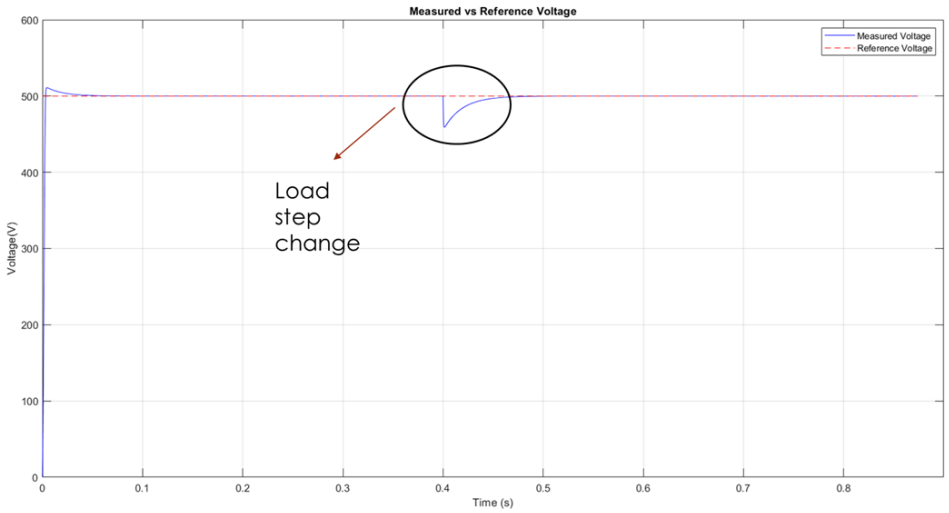

Figure 5.3: Measured output voltage vs. reference voltage during load transient at $t = 0.4$ s.

Figure 5.3 illustrates how the simulation precisely tracks the output voltage in relation to the 500 V reference voltage. A brief transient deviation is produced when a step load adjustment is provided at $t = 0.4$ s, as seen in Figure 5.3. The output voltage swiftly returns to the reference value when the controller reacts efficiently, demonstrating that the closed-loop control system functions as planned and maintains voltage regulation in dynamic situations.

Similarly, the simulation results also demonstrate accurate current control. The measured inductor current closely follows the reference or theoretical current of 20 A under nominal conditions. At $t = 0.4$ s, a step change in load is applied, and the current transitions to follow the new reference of 40 A. As illustrated in Figure 5.4, the controller ensures fast and stable tracking of the desired current, indicating effective closed-loop current regulation. The simulated waveforms of the primary voltage, secondary voltage, and inductor current of the DAB converter are shown in Figure 5.5. As observed, the results closely match the expected theoretical waveforms of a Dual

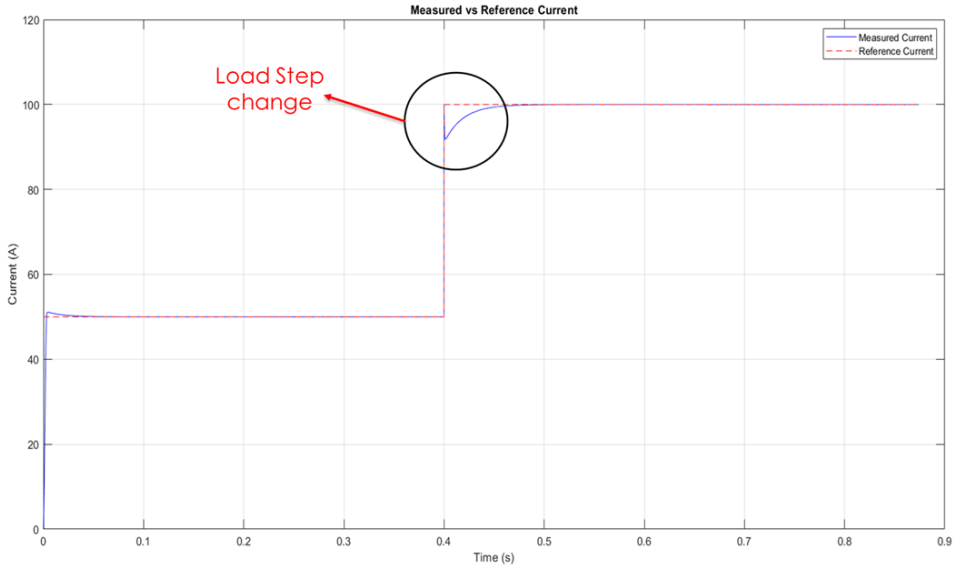

Figure 5.4: Measured output current vs. reference current during load transient at $t = 0.4$ s.

Active Bridge converter, thereby validating the accuracy of the model and the correctness of the implemented control strategy.

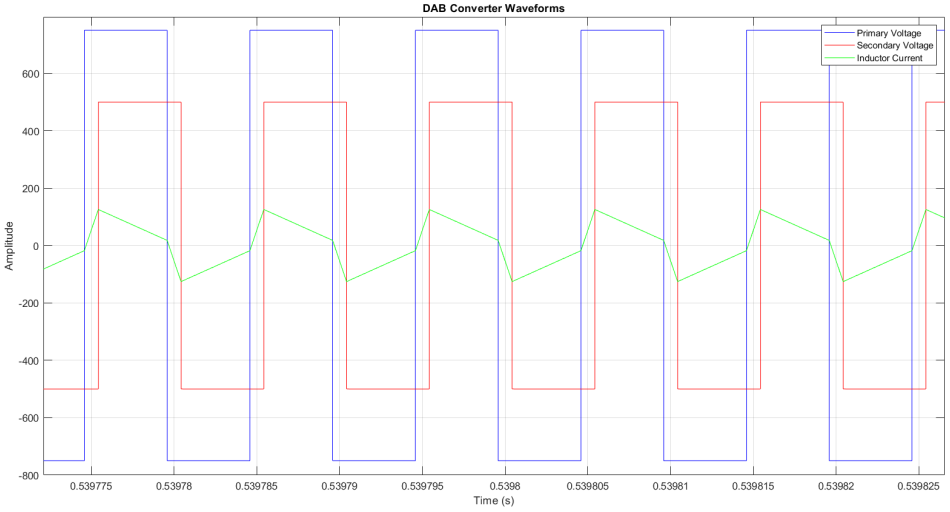

Figure 5.5: Simulated primary voltage, secondary voltage, and inductor current waveforms of the DAB converter.

5.2 Modular DAB simulation

5.2.1 Open loop control of Modular DAB

Table 5.2: Modular Converter Parameters

Parameters	**Symbol**	**Value**
Power rating of each converter	P	10kW
Total Input Voltage	V_{in}	2250 V
Number of Modules	N	3
Output Voltage range	V_o	300-500 V
Leakage Inductance	L	0.0102 mH
Parasitic Resistance	R_p	$200m\Omega$
Switching Frequency	f_s	100 kHz
Transformer Ratio	n	0.5
Input Capacitance	Ci	470 μF
Output Capacitance	Co	950 μF
Load Resistance	R	10Ω, 10Ω

An open-loop simulation was conducted for a three-module DAB system, where each module operates with a fixed normalized phase shift of $D = 0.25$. Figure 5.6 presents the comparison between the reference voltage and the measured output voltage of the converter. It can be observed that in the absence of closed-loop control, the output voltage does not perfectly track the reference, indicating steady-state error due to fixed duty operation.

Additionally, the voltage and current waveforms of one representative DAB module are shown in Figure 5.7. These waveforms are consistent with the expected theoretical behavior for a DAB converter operating under open-loop conditions with $D = 0.25$.

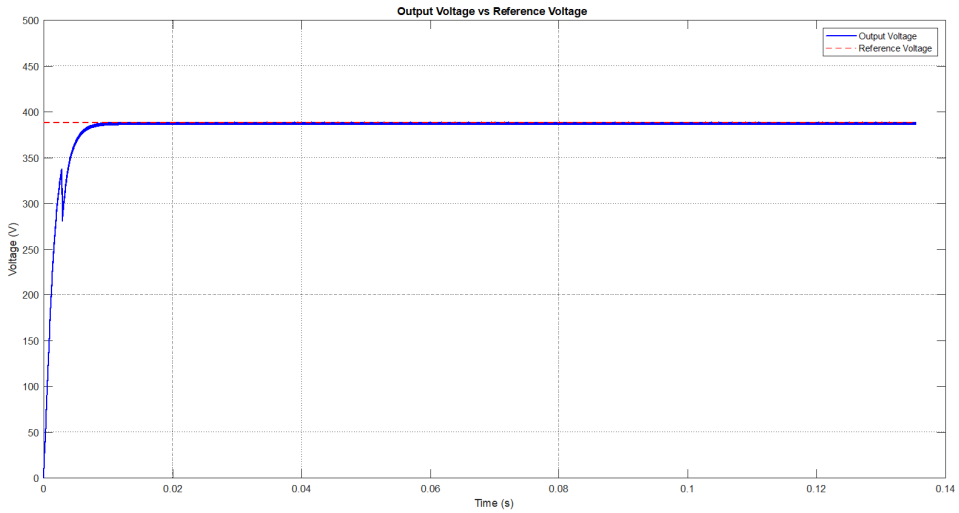

Figure 5.6: Reference vs. output voltage in open-loop simulation of 3-module DAB with $D = 0.25$.

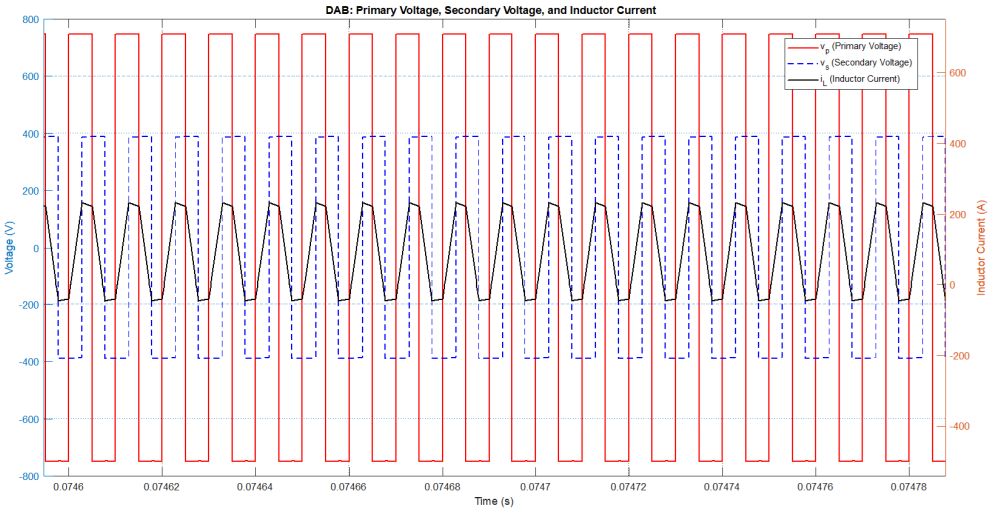

Figure 5.7: Primary voltage, secondary voltage, and inductor current waveforms of one DAB module in open-loop.

5.2.2 Effect of Leakage Inductance Mismatch on Inductor Current

To evaluate the impact of parameter mismatch, an open-loop simulation was carried out by introducing variations in the leakage inductance values of module 2 and module 3. Specifically, the leakage inductance of module 2 was increased by 10%, while that of module 3 was increased by 12%, relative to the nominal value used in module 1. The resulting inductor currents are shown in Figure 5.8.

As seen in the plot, the mismatch in leakage inductance leads to an imbalance in the current sharing among the three DAB modules. Module 1, with the nominal inductance, carries a higher portion of the load current, while modules 2 and 3 carry proportionally less. This demonstrates the sensitivity of current distribution to component mismatches in open-loop operation, emphasizing the importance of tight parameter matching or the need for closed-loop current balancing mechanisms in modular DAB systems.

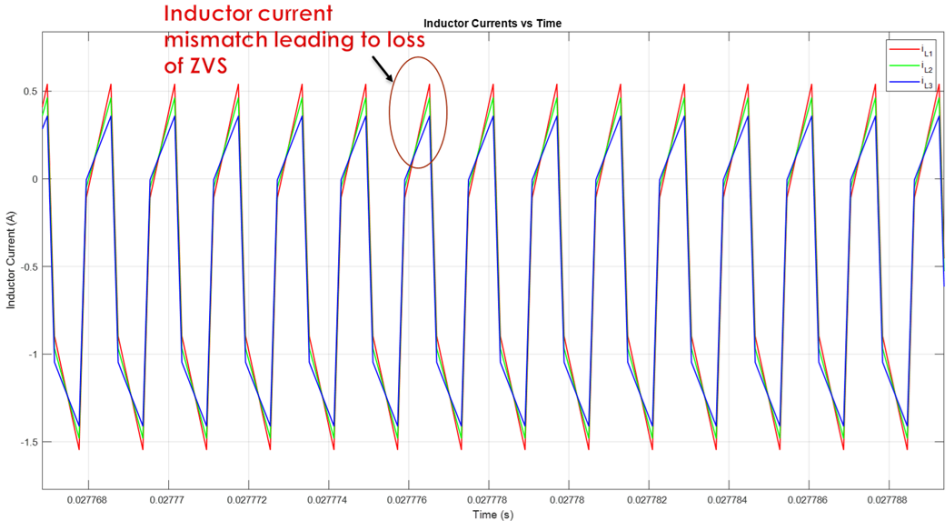

Figure 5.8: Inductor current mismatch due to 10% and 12% increase in leakage inductance of module 2 and module 3, respectively.

5.2.3 Analytical Verification Average Model of 3 Module ISOP DAB

To analytically verify the average model of the three-module ISOP DAB converter, frequency domain analysis was conducted. The Bode plot of the small-signal transfer function from normalized time shift $\hat{d}_1$ to output voltage $\hat{v}_o$ was generated, as shown in Figure 5.9.

The plot confirms the stability of the system. The phase margin is approximately 98.6° at a crossover frequency of 2.2×10^4 rad/s, while the gain margin is infinite, indicating robust phase and gain stability. These results validate the correctness of the derived average model and its suitability for control design in the ISOP DAB configuration.

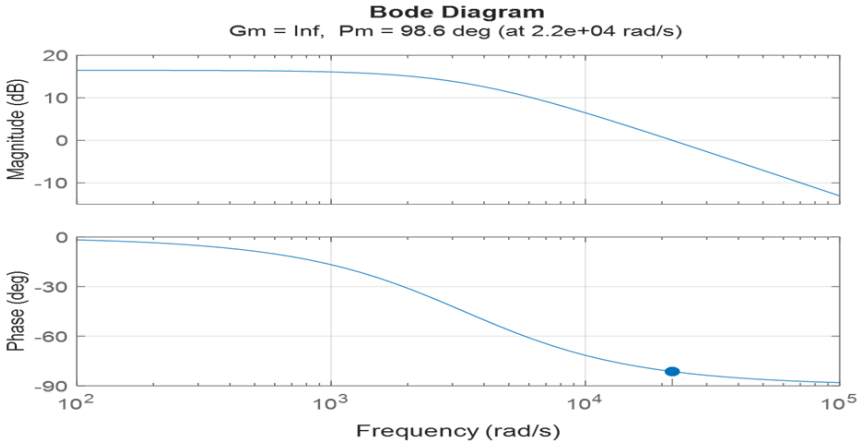

Figure 5.9: Bode plot of output voltage $\hat{v}_o$ with respect to normalized time shift $\hat{d}_1$ for the average model of the 3-module ISOP DAB system

In addition to output voltage validation, the frequency response of the input voltage perturbation $\hat{v}_{i1}$ with respect to the normalized time shift $\hat{d}_1$ was also analyzed. The resulting Bode plot is shown in Figure 5.10.

The plot indicates a constant positive phase and a monotonically decreasing gain, which is consistent with theoretical predictions. The phase margin is reported as $-90°$ at a gain crossover frequency of 992 rad/s. This confirms the accuracy and frequency-domain behavior of the transfer function from $\hat{d}_1$ to $\hat{v}_{i1}$ for the average model.

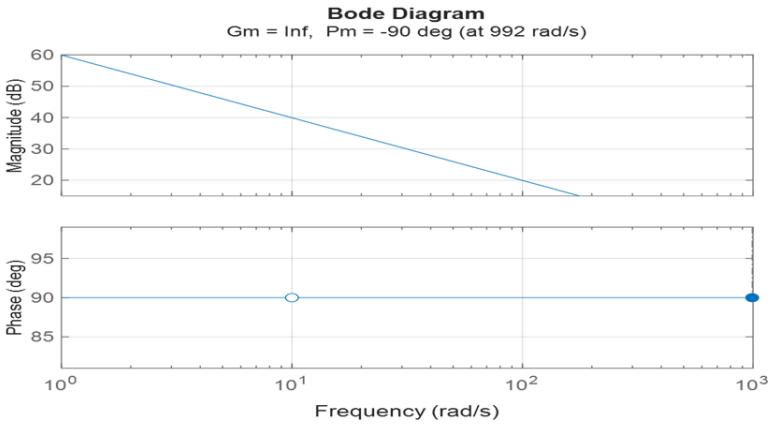

Figure 5.10: Bode plot of input voltage perturbation $\hat{v}_{i1}$ with respect to normalized time shift $\hat{d}_1$ in the average model of the 3-module ISOP DAB system.

5.2.4 Closed loop control of Modular DAB

Closed-Loop Simulation Using Decoupled Control

As demonstrated in Chapter 4, the closed-loop simulation of the three-module DAB converter is carried out using the decoupled control strategy. The simulation is implemented in MATLAB/Simulink, and the corresponding Simulink model with decoupled control loops is shown in Figure 5.11.

Closed-Loop Simulation Using Decoupled Control

As demonstrated in Chapter 4, the closed-loop simulation of the three-module DAB converter is carried out using the decoupled control strategy. The simulation is implemented in MATLAB/Simulink, and the corresponding Simulink model with decoupled control loops is shown in Figure 5.11.

The output voltage response in comparison with the reference voltage is illustrated in Figure 5.12. It can be observed that the output voltage closely follows the reference of 500 V under steady-state conditions. Furthermore, when a step change in load is introduced, a short transient occurs, after which the controller restores the output voltage to its reference level, demonstrating the effectiveness of the closed-loop regulation.

In addition, the output current is compared against the theoretical current in Figure 5.13. The current tracking performance is precise, and the measured current follows the theoretical value both before and after the load change, confirming the accuracy of current regulation in the system.

The waveforms of the primary and secondary voltages, along with the inductor current of one DAB module, are shown in Figure 5.14. These signals closely resemble the expected theoretical waveforms, further validating the system modeling and control design.

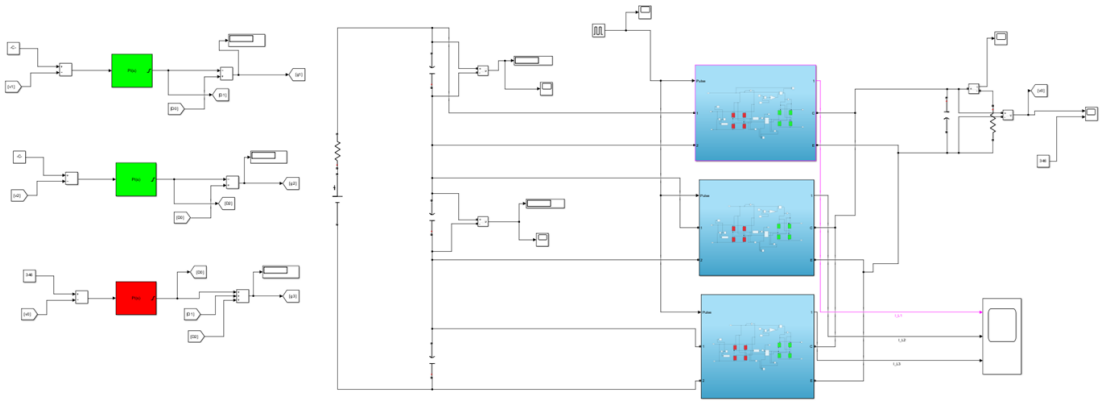

Figure 5.11: Simulink model of the three-module DAB converter with decoupled control loops.

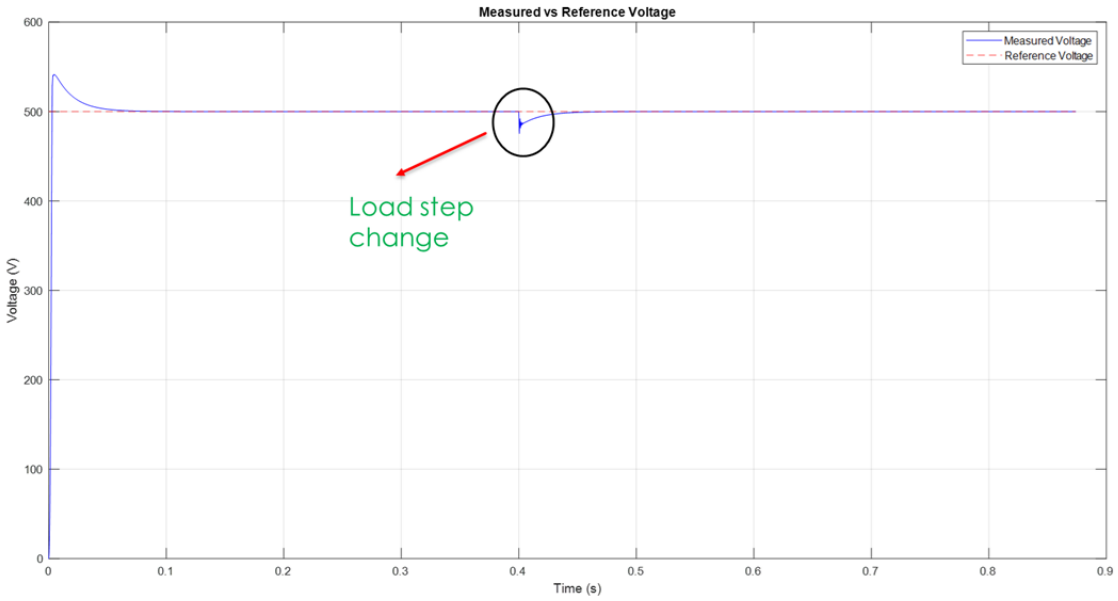

Figure 5.12: Closed-loop output voltage vs. reference voltage under step load change.

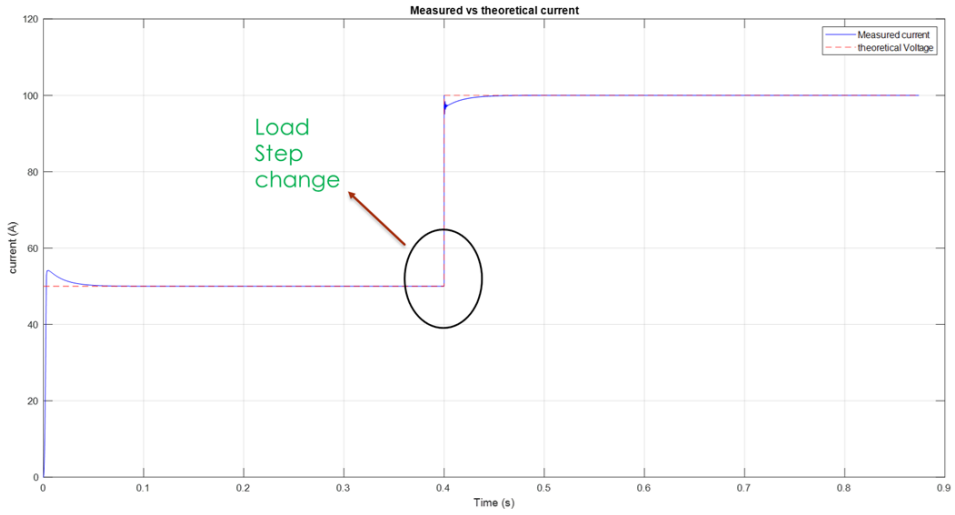

Figure 5.13: Measured output current vs. theoretical current under closed-loop operation.

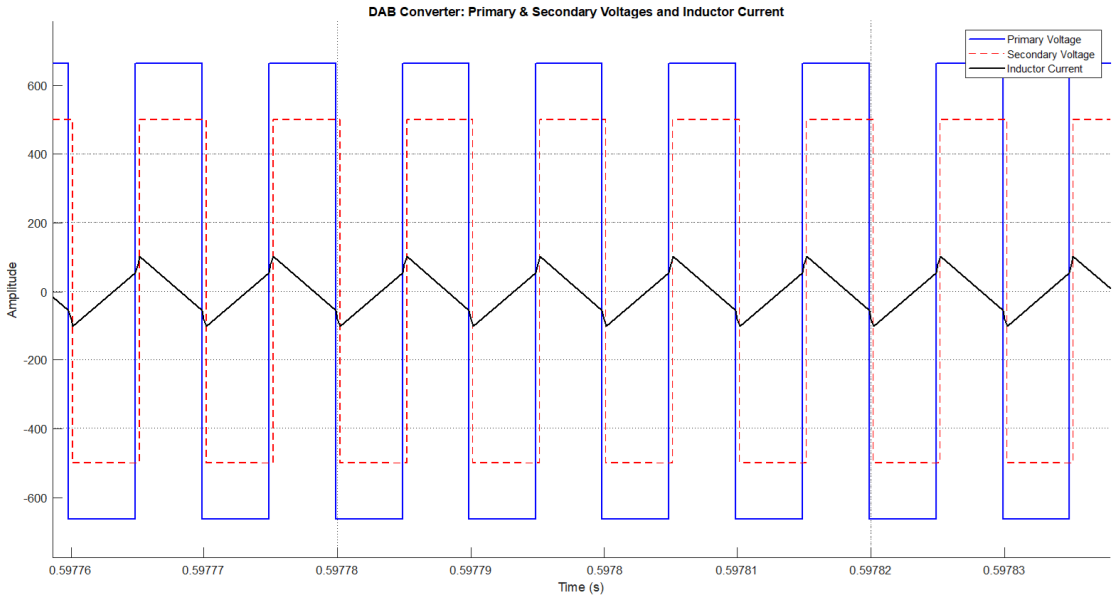

Figure 5.14: Primary voltage, secondary voltage, and inductor current waveforms of one DAB module under closed-loop control.

5.3 LTspice Simulation of 2 Module ISOP DAB

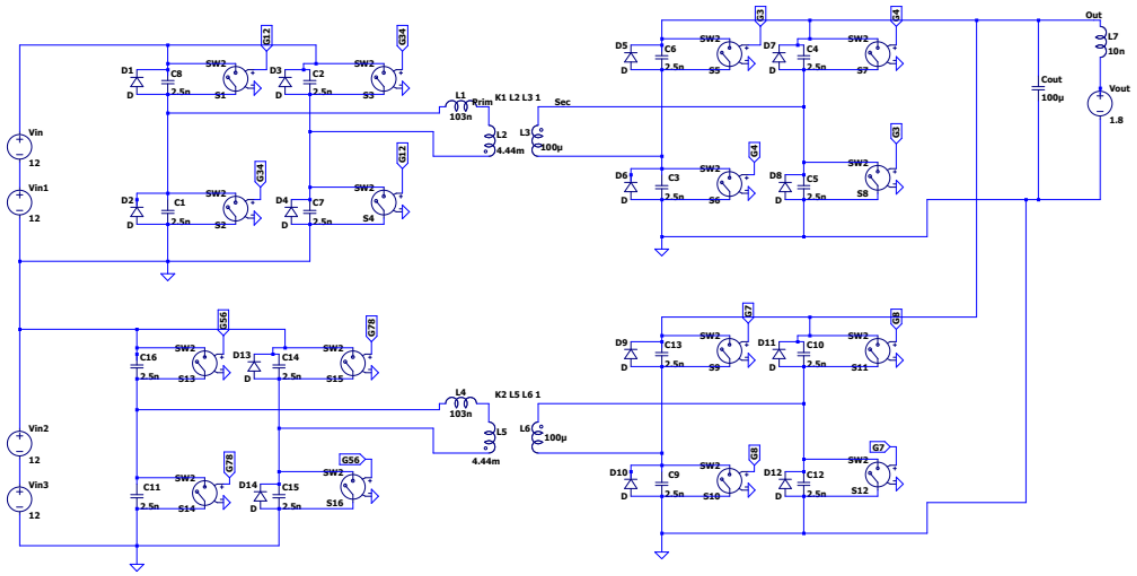

Figure 5.15: LTspice schematic of the 2 Module ISOP converter

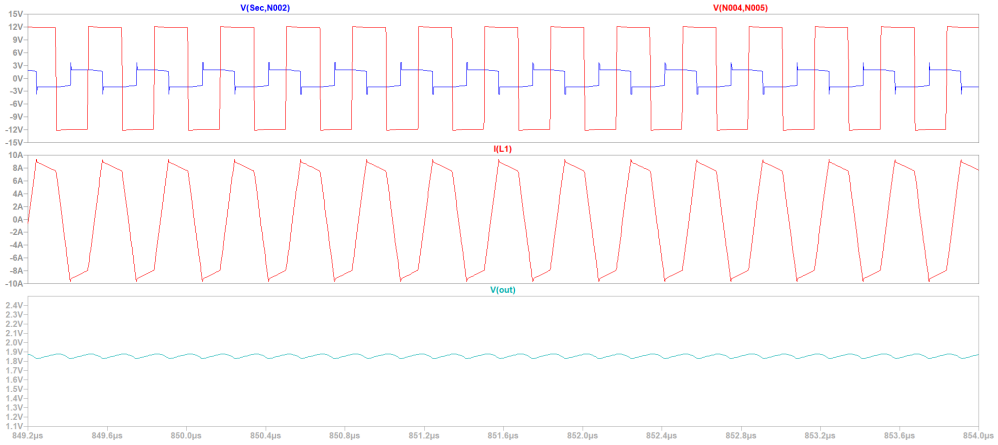

Figure 5.16: Simulation results of the ISOP converter in LTspice showing voltage and current waveforms.

The LTspice simulation shown here represents the proposed converter architecture for achieving a step-down conversion from 48 V to 1.8 V using the Input-Series Output-Parallel (ISOP) topology. The converter operates at a switching frequency of f_{sw} = 100 kHz. As illustrated in Figure 5.15, the ISOP structure consists of two identical

converter branches. The inputs of these branches are connected in series, while the outputs are connected in parallel.

Ideal gate drivers are assumed in the simulation, and appropriate phase shift control is incorporated to reflect realistic modulation behavior. The complete simulated circuit topology is depicted in Figure 5.15.

The simulation results, including key waveforms such as voltage, current, and switching behavior, are presented in Figure 5.16. These results verify the correct operation of the ISOP converter and its suitability for high step-down ratio applications.

Chapter 6

Conclusion and Future work

6.0.1 Conclusion

This thesis began with an in-depth review of a range of DC-DC converter topologies, providing the necessary foundation for a detailed investigation of the Dual Active Bridge (DAB) converter. The DAB topology is particularly important due to its inherent ability to facilitate bidirectional power flow and its integration of galvanic isolation via a high-frequency transformer. Operating at elevated switching frequencies allows for the use of smaller, lighter magnetic components and filters, thereby enhancing the converter's overall efficiency. ‘ In our thesis, we used fourier series analysis to model the Dual Active Bridge (DAB) converter. From this, we were able to determine the small signal behavior of the converter. Based on this research, we designed a PI controller to achieve a closed loop design.

In this thesis we also studied the modeling, analysis, and closed-loop control design of a three-module Dual Active Bridge (DAB) converter system operating under an Input-Series Output-Parallel (ISOP) configuration. The average model for Input-Series Output-Parallel (ISOP) Dual Active Bridge (DAB) was developed to understand the dynamic behavior and interdependencies of the modular system. The decoupled

control strategy was implemented to transform the MIMO system into independent SISO control loops, significantly simplifying controller design.

Simulation studies conducted in MATLAB/Simulink validated the effectiveness of the proposed control architecture. The closed-loop system demonstrated accurate voltage and current tracking under nominal and transient conditions, while the average model was verified analytically through frequency-domain analysis using Bode plots. Additionally, open-loop and mismatch simulations provided insights into system sensitivity and the importance of parameter matching.

The results confirm that the proposed modular and decoupled control strategy ensures stable, scalable, and efficient power conversion suitable for low-voltage, high-current applications such as data centers and telecom systems.

6.0.2 Future Work

While this thesis has focused on the modeling, control, and simulation of a modular Dual Active Bridge (DAB) system under an ISOP (Input-Series Output-Parallel) configuration, several promising directions remain open for future exploration.

- **Extension to Other Modular Topologies:** Future studies can investigate alternative modular DAB configurations such as IPOP (Input-Parallel Output-Parallel) and IPOS (Input-Parallel Output-Series), to assess their performance under different voltage and current scaling requirements.

- **Generalized Control for Parameter Variations:** The developed control strategy can be extended to handle systems with non-identical module parameters. Real-world implementations often exhibit variations in leakage inductance, input capacitance, or transformer turns ratios. A more generalized control framework that ensures robust performance under such mismatches would be valuable.

- **Decentralized and Adaptive Control:** Future work can explore adaptive or decentralized control techniques to reduce reliance on central coordination. Such approaches may enhance scalability and fault tolerance, particularly in large modular systems.

- **AI-Based Predictive Control:** With the growing capability of artificial intelligence, AI-based predictive control strategies—such as reinforcement learning, neural network-based model predictive control (MPC), or data-driven optimization—can be investigated to enable more intelligent and adaptive power management across modular converters.

- **Hardware Implementation and Experimental Validation:** The proposed control methods can be implemented on real-time hardware platforms (e.g., DSP, FPGA, or microcontroller) for experimental validation. This would confirm the practical feasibility of the control design and its performance under real operating conditions, including dynamic load changes and non-idealities.

References

[1] S. A. Gorji, H. G. Sahebi, M. Ektesabi, and A. B. Rad, "Topologies and control schemes of bidirectional dc–dc power converters: An overview," *IEEE access*, vol. 7, pp. 117 997–118 019, 2019.

[2] T. Instruments, "Design guide: Tida-010054 bidirectional, dual active bridge reference design for level 3 electric vehicle charging stations, 2022."

[3] P. Zumel, L. Ortega, A. Lazaro, C. Fernandez, and A. Barrado, "Control strategy for modular dual active bridge input series output parallel," in *2013 IEEE 14th Workshop on Control and Modeling for Power Electronics (COMPEL)*. IEEE, 2013, pp. 1–7.

[4] S. Gorji, M. Ektesabi, and J. Zheng, "Isolated switched-boost push–pull dc–dc converter for step-up applications," *Electronics Letters*, vol. 53, no. 3, pp. 177–179, 2017.

[5] A. Aboulnaga and A. Emadi, "Performance evaluation of the isolated bidirectional cuk converter with integrated magnetics," in *2004 IEEE 35th Annual Power Electronics Specialists Conference (IEEE Cat. No. 04CH37551)*, vol. 2. IEEE, 2004, pp. 1557–1562.

[6] X. Xu, A. M. Khambadkone, and R. Oruganti, "A soft-switched back-to-back bi-directional dc/dc converter with a fpga based digital control for automotive applications," in *IECON 2007-33rd Annual Conference of the IEEE Industrial Electronics Society*. IEEE, 2007, pp. 262–267.

[7] P. He and A. Khaligh, "Comprehensive analyses and comparison of 1 kw isolated dc–dc converters for bidirectional ev charging systems," *IEEE Transactions on Transportation electrification*, vol. 3, no. 1, pp. 147–156, 2016.

[8] Y. Du, S. Lukic, B. Jacobson, and A. Huang, "Review of high power isolated bi-directional dc-dc converters for phev/ev dc charging infrastructure," in *2011 IEEE Energy Conversion Congress and Exposition*. IEEE, 2011, pp. 553–560.

[9] A. Chub, D. Vinnikov, R. Kosenko, E. Liivik, and I. Galkin, "Bidirectional dc–dc converter for modular residential battery energy storage systems," *IEEE Transactions on Industrial Electronics*, vol. 67, no. 3, pp. 1944–1955, 2019.

[10] G. Ortiz, H. Uemura, D. Bortis, J. W. Kolar, and O. Apeldoorn, "Modeling of soft-switching losses of igbts in high-power high-efficiency dual-active-bridge dc/dc converters," *IEEE Transactions on Electron Devices*, vol. 60, no. 2, pp. 587–597, 2012.

[11] A. A. Chamyousefali, "Analysis of dual active bridge converter," Master's thesis, Politecnico di Milano, 2022.

[12] S. Joarder, A. Ghosh, S. Banerjee, C. Sain, and F. Ahmad, "Harmonic modelling and control of dual active bridge converter for dc microgrid applications," *Energy Reports*, vol. 12, pp. 52–74, 2024.

[13] G. C. Goodwin, S. F. Graebe, M. E. Salgado *et al.*, *Control system design*. Prentice Hall Upper Saddle River, 2001, vol. 240.

[14] R. C. D. R. H. Bishop, *Modern control systems*, 2011.

[15] B. Friedland, *Control system design: an introduction to state-space methods*. Courier Corporation, 2012.

[16] A. Rodriguez, A. Vazquez, D. G. Lamar, M. M. Hernando, and J. Sebastian, "Different purpose design strategies and techniques to improve the performance of a dual active bridge with phase-shift control," *IEEE Transactions on Power Electronics*, vol. 30, no. 2, pp. 790–804, 2014.

[17] P. Zumel, L. Ortega, A. Lazaro, C. Fernandez, A. Barrado, A. Rodriguez, and M. M. Hernando, "Modular Dual-Active bridge converter architecture," *IEEE Trans. Ind. Appl.*, vol. 52, no. 3, pp. 2444–2455, May 2016.

[18] X. Ruan, W. Chen, L. Cheng, C. K. Tse, H. Yan, and T. Zhang, "Control strategy for input-series–output-parallel converters," *IEEE Transactions on Industrial Electronics*, vol. 56, no. 4, pp. 1174–1185, 2008.